Impact of Medium Scale Heterogeneities on CO_2 Storage

A Comparative Study of Model Complexity and Short Term Evolution in the Pano Flood Tidal Delta

Longyu Shi

TU Delft

Impact of Medium Scale Heterogeneities on CO_2 Storage

A Comparative Study of Model Complexity and Short Term Evolution in the Pano Flood Tidal Delta

Thesis report

by

Longyu Shi

to obtain the degree of Master of Science
at the Delft University of Technology
to be defended publicly on November 18, 2025 at 13:30

Thesis committee:

Chair:	Prof. Dr. Allard W. Martinius
Supervisors:	Prof. Dr. Sebastian Geiger
	Dr. Anne Pluymakers
Project Duration:	December, 2024 - November, 2025
Student number:	5862116

An electronic version of this thesis is available at `http://repository.tudelft.nl/`.

Faculty of Civil Engineering and Geosciences · Delft University of Technology

Abstract

This study [1] quantifies the impact of mesoscale geological heterogeneity on CO_2 storage behavior, using the Pano flood-tidal delta as a case study. A hierarchical workflow was employed, progressing from simple to complex static modeling (L1 to L4) based on outcrop interpretation, followed by flow diagnostics analysis. The results reveal a non-linear relationship between model complexity and system behavior. The mesoscale architecture (L2) primarily controls early CO_2 breakthrough risk, whereas the sub-lobe scale heterogeneity (L3) is crucial for reliably predicting long-term storage performance and sweep efficiency.

A key insight from this work is that **the level of model complexity systematically biases the simulated flow narrative**. Consequently, there is no single ”correct” model; instead, the choice of complexity inherently pre-selects which aspects of storage behavior (e.g., early risk vs. long-term efficiency) will be most accurately represented. This provides a decision-making framework for CO_2 storage projects, demonstrating that distinct optimal levels of model complexity exist for specific engineering objectives, such as using L2 for risk identification and L3 for performance prediction—thereby guiding more effective and intentional model deployment.

[1] **Acknowledgement of AI Assistance:** This work was completed with the support of DeepSeek AI, which was used exclusively for language polishing and editing to improve clarity and fluency. The intellectual work, including the research design, data interpretation, result synthesis, and the formulation of conclusions, remains entirely the responsibility of the author.

Acknowledgement

First and foremost, I would like to express my heartfelt gratitude to my thesis supervisors, Professor Allard W. Martinius and Professor Sebastian Geiger, for their patient guidance, insightful feedback, and continuous support throughout this project. Your encouragement helped me navigate not only academic challenges but also moments of self-doubt, and your expertise has deeply enriched the development of this research.

I would also like to extend my sincere appreciation to Dr. Anne Pluymakers for serving on my thesis defence committee and for her valuable comments and suggestions, which greatly strengthened this work. I am equally grateful to Associate Professor Joep Storms and Dr. Timothy Baars, whose support and collaboration played an important role in the successful completion of this project.

To my family, thank you for being my steady source of strength during this long journey. Your understanding and kindness, especially during difficult times, meant more to me than words can fully express.

Finally, I would like to share a few words about what this academic journey has meant to me.

During my time at Delft, I faced setbacks I had spent many years trying to avoid—delays, failures, emotional turbulence, and moments of profound self-doubt. Yet it was through confronting these experiences that I learned something fundamental: failure is not a verdict, but a passage.

These moments encouraged me to re-examine beliefs I once accepted without question—the pursuit of perfection, the fear of falling short, and the quiet yet persistent pressure of performance-oriented education. In this process, I turned to psychology and came to better understand how external expectations and our own inner narratives can quietly shape us. Through volunteering and conversations with students temporarily stepping away from school due to emotional difficulties, I recognized their struggles—and, in many ways, glimpsed a younger version of myself.

I am grateful that I will soon begin work in a field connected to my studies—a continuation of this journey, and a chance to find meaning in new uncertainties, challenges, and responsibilities. At the same time, I hope to continue contributing to youth mental-health support, walking alongside those navigating emotional lows, and, in a way, offering the companionship I once needed myself.

These years have shown me that progress is rarely linear, but choosing to face what we fear can open paths to understanding—and perhaps, to healing.

Thank you to everyone who walked with me, in ways both great and small.

Longyu Shi Delft, November 2025

Contents

List of Figures

List of Tables

1 Introduction

1.1. Background

The world has entered a new climate reality, moving past the 1.5°C threshold and rapidly approaching a series of disastrous tipping points that threaten the stability of key planetary systems [1]. In this urgent context, Carbon capture and storage (CCS) has emerged as a crucial technological pathway for climate change mitigation and the pursuit of net-zero emissions [2]. The overarching objective of CCS is the secure and permanent immobilization of billions of tons of CO_2 in deep geological formations, such as saline aquifers and depleted hydrocarbon reservoirs [3, 4]. However, a significant gap persists between theoretical storage potential and practical, certifiable capacity, largely due to uncertainties in predicting the long-term migration and trapping of the CO_2 plume within inherently heterogeneous subsurface environments [5, 6]. Accurately forecasting plume behavior is not merely an academic exercise; it is a fundamental prerequisite for demonstrable storage integrity, robust risk assessment, and regulatory approval.

The security and efficacy of geological CO_2 storage are fundamentally governed by processes that operate across a vast spectrum of spatial scales [7, 8]. An integrated understanding, from the pore to the field, is essential, as heterogeneity at each scale distinctly influences the dominant trapping mechanisms [9, 7]. The following synthesis leverages the terminology and scale classifications established in these reviews to clarify these critical linkages (Figure 1.1).

1. **At the Pore Scale:**

   The physics of fluid displacement are controlled by interfacial tension, wettability, and the geometry of the pore space. During imbibition, the receding CO_2 plume is disconnected into immobile ganglia through the process of snap-off, forming the basis of residual trapping [7]. X-ray microtomography studies at reservoir conditions have confirmed that this process can trap significant quantities of CO_2, with residual saturations characteristic of water-wet systems [10]. This trapping mechanism is pervasive and provides the first line of immobilization following the buoyant migration of the plume.

2. **At the Core to Mesoscale:**

   This is the central scale of investigation for this work. A different capillary-driven process emerges, driven by the sedimentary architecture of the rock. Heterogeneities such as cross-stratified bedsets, laminations, and mud drapes create a structured mosaic of capillary entry pressures [9]. When the buoyant pressure of a continuous CO_2 body is lower than the entry pressure of an overlying finer-grained layer, the CO_2 is immobilized in a process known as capillary pinning (local capillary trapping) [11, 12] (Figure 1.2). Critically, the low-permeability layers responsible for this trapping are often the very intervals excluded as ”non-reservoir” in traditional hydrocarbon models [13]. Their omission in CO_2 storage simulations invalidates forecasts of plume migration and trapping capacity, leading to a potentially severe overestimation of risk.

3. **At the Reservoir Scale:**

   At the reservoir scale, the collective impact of all smaller-scale processes is integrated into the plume’s macroscopic behavior [9]. The distribution of mesoscale heterogeneities controls the plume’s migration pathway, determining its contact area with brine (influencing dissolution trapping) and its pressure on the primary seal (defining structural trapping) [14, 15]. Models that fail to represent the

capillary heterogeneity introduced at the mesoscale will be inherently incapable of predicting this integrated plume response, leading to potentially severe errors in capacity and risk assessment [13].

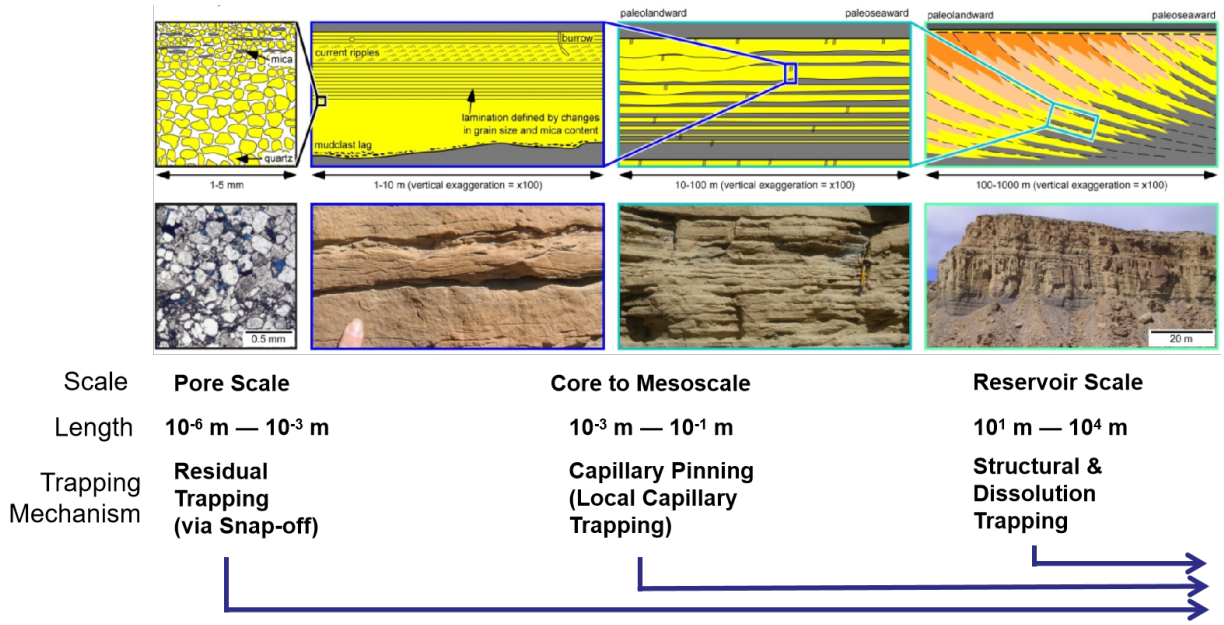

Figure 1.1: The multi-scale control of geological heterogeneity on CO_2 trapping, adapted from the hierarchical framework of Zhang et al. (2025).

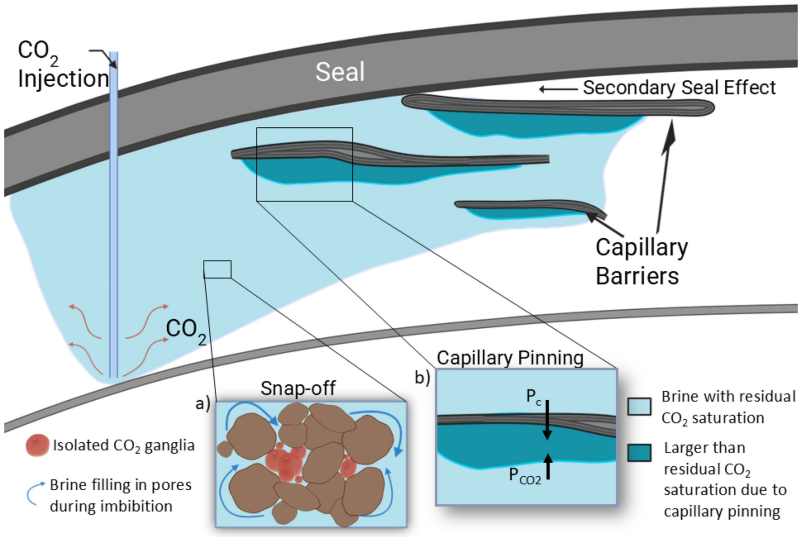

Figure 1.2: Trapping mechanisms at the core-to-mesoscale (modified from Zhang et al. (2025), after Gershenzon et al. (2017)). (a) Snap-off trapping at the pore scale immobilizes CO_2 as disconnected ganglia. (b) Capillary pinning at the mesoscale immobilizes continuous CO_2 phases beneath capillary barriers, leading to higher local saturations. This mesoscale process is a key control on plume evolution in heterogeneous deposits.

A central challenge in predicting storage performance lies in accurately representing this complexity in models. Oversimplified models, particularly those repurposed from hydrocarbon production, which often employ net cut-offs and simplified fault representations, fail to capture critical flow barriers and the role of low-permeability layers in capillary trapping, leading to overly optimistic forecasts of plume migration and containment [13]. Conversely, the pursuit of ”full physics” models that explicitly capture every detail

from pore to basin scale can become computationally prohibitive; there is currently no consensus on the optimal level of model complexity required to make reliable storage forecasts [13]. This trade-off highlights a critical knowledge gap: the lack of a systematic, quantitative understanding of how different hierarchies of geological heterogeneity impact CO_2 storage performance.

1.2. Research Question

To address the identified challenge, this study is guided by the following two research questions:

Research Question 1

How can medium-scale discrete rock heterogeneities in flood-tidal delta deposits be effectively represented in static geological models for CO_2 storage applications?

Research Question 2

How do medium-scale rock heterogeneities in flood-tidal delta deposits influence the CO_2 storage evolution as model complexity increases at short (1 to 100 years) time scales?

1.3. Thesis Structure

This study followed a systematic workflow to quantify how hierarchical geological heterogeneity affects CO_2 storage performance. The integrated process, summarized in Figure 1.3, progressed through three sequential phases:

- **Phase I: Geological Foundation & Conceptual Modeling (Chapters 2 & 5):** The Pano outcrop was systematically analyzed and interpreted to define a hierarchy of architectural elements (L1-L5). This established the conceptual geological blueprint for all subsequent modeling.
- **Phase II: Numerical Model Construction & Parameterization (Chapters 3, 4 & 6):** The conceptual blueprint was translated into a suite of four digital static models (L1-L4) with increasing complexity. These models were populated with petrophysical properties based on a calibrated subsurface analogue.
- **Phase III: Dynamic Analysis & Synthesis (Chapters 7, 8 & 9):** Flow diagnostics simulations were performed on all models. The comparative analysis of results identified how each scale of heterogeneity controls CO_2 behavior, culminating in a conceptual framework for selecting optimal model complexity.

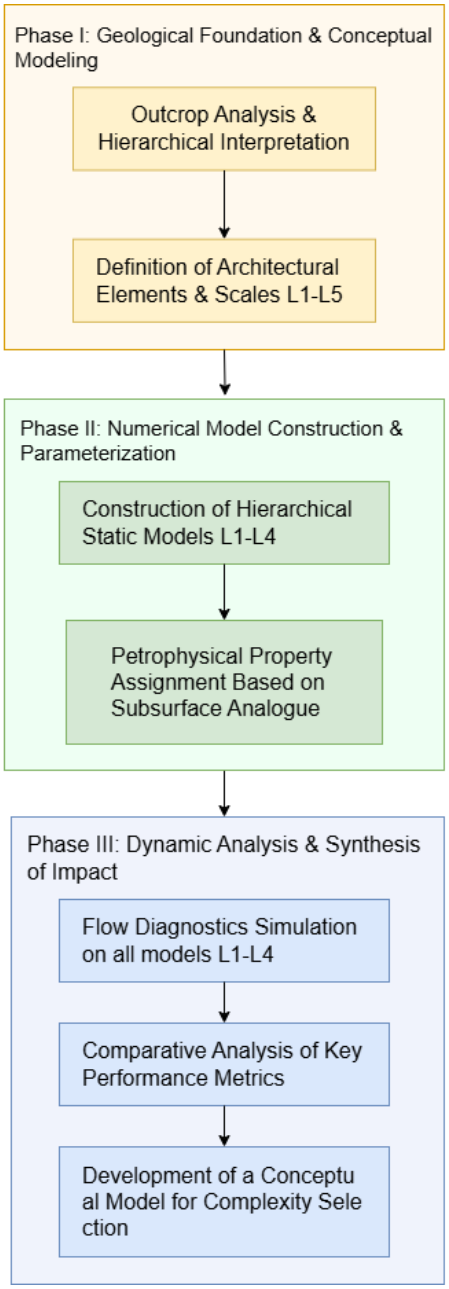

Figure 1.3: Systematic workflow of the hierarchical modeling and analysis procedure used in this study.

2

Geological Background

2.1. Regional Geological Setting

This section establishes the geological context of the study, which focuses on the flood-tidal delta deposits of the Pano Formation exposed near the village of Pano. The objective is to situate this specific depositional element within its broader geographical, tectonic, stratigraphic, and depositional framework.

2.1.1. Geographical Location

The study focuses on the exposed flood-tidal delta deposits of the Pano Formation, located northeast of the village of Pano in the southern Pyrenees, Spain (Figure 2.1 B). The Pano Formation as a whole is exposed within a north-south-oriented, 8 km long and 3-4 km wide depositional belt. This belt extends westward from a line connecting the villages of Graus, Ejep, and the Pico de Campanué, with its northern limit located approximately 3 km NNE of Pano, where it transitions into the distal facies of the Campanué fan delta [16]. The specific research target—the Pano flood-tidal delta—is exposed in three dimensions across a series of cliff faces (Cliff 1 to 3 in Figure 2.2 A) and corresponds to parasequence 1.1 of Figure 2.1 A. The architectural analysis presented in this study is primarily based on the detailed examination of the NE-SW-oriented Panel C in Figure 2.2.

2.1.2. Tectonic Framework

The Pano Formation was deposited during the Middle Lutetian within the South-Pyrenean Foreland Basin, a flexural basin formed by the Late Cretaceous to Miocene collision between the Iberian and Eurasian plates [17]. The structural architecture is characterized by south-verging thrust sheets. The study area is situated within the Gavarnie-Sierras thrust sheet, which was being transported in the footwall of the major, actively advancing Montsec-Peña Montañesa thrust sheet [18]. This part of the orogen is characterized by a thin-skinned structural style, with the Mesozoic and Cenozoic cover sequences decoupled from the basement along the Triassic evaporites [17, 19].

The first-order control on the local palaeogeography was the syn-sedimentary growth of the Mediano anticline. This structure is a large detachment fold cored by up to 3 km of Triassic evaporites and shales [18, 20]. Its growth, active from the early Lutetian to Bartonian, created a positive structural high to the south of the study area, restricting the depositional system and fostering the development of a protected, shallow-marine embayment—the 'Pano Bight' [16]. The Mediano anticline is part of the Ainsa Oblique Zone, a set of N-S trending folds at the western edge of the South-Pyrenean Central Salient. Paleomagnetic and structural studies demonstrate that this oblique zone underwent significant clockwise vertical-axis rotations of up to 70° during the Eocene, which directly controlled the spatio-temporal evolution of the depositional systems [21, 19].

2.1.3. Stratigraphic Framework

The Pano Formation is an approximately 170 m thick overall transgressive coastal succession ([22, 16, 23]). It was deposited at the crossroads of two sediment delivery systems: the Campanué fan delta, located to the northeast, which served as the main sediment source, and the northern part of the extensive axial Capella fluvial system from the east-southeast [16].

Donselaar (1996) recognized two main stratigraphic intervals separated by an unconformity interpreted

as a sequence boundary (Figure 2.1 A):

- **Sequence 1 (Lower Interval):** This approximately 110 m thick unit is intermittently exposed along the entire 8 km long outcrop belt. It records the last prograding phase of the Campanué fan delta and the subsequent development of three successive, retrograding barrier-lagoon systems (the Pano, Panillo, and Grustán barriers).
- **Sequence 2 (Upper Interval):** This overlying unit is about 60 m thick and is only exposed near the village of Grustán.

The formation is of Middle Lutetian age, with a duration of approximately 1.2 Myr from 43.2 Ma to 42.0 Ma ([24, 25, 26]. Deposition occurred during the last phase of the Paleocene-Eocene Hothouse period, which was characterized by long-term cooling interrupted by the transient Middle Eocene Climatic Optimum, with estimated global average temperatures reaching 23°C.

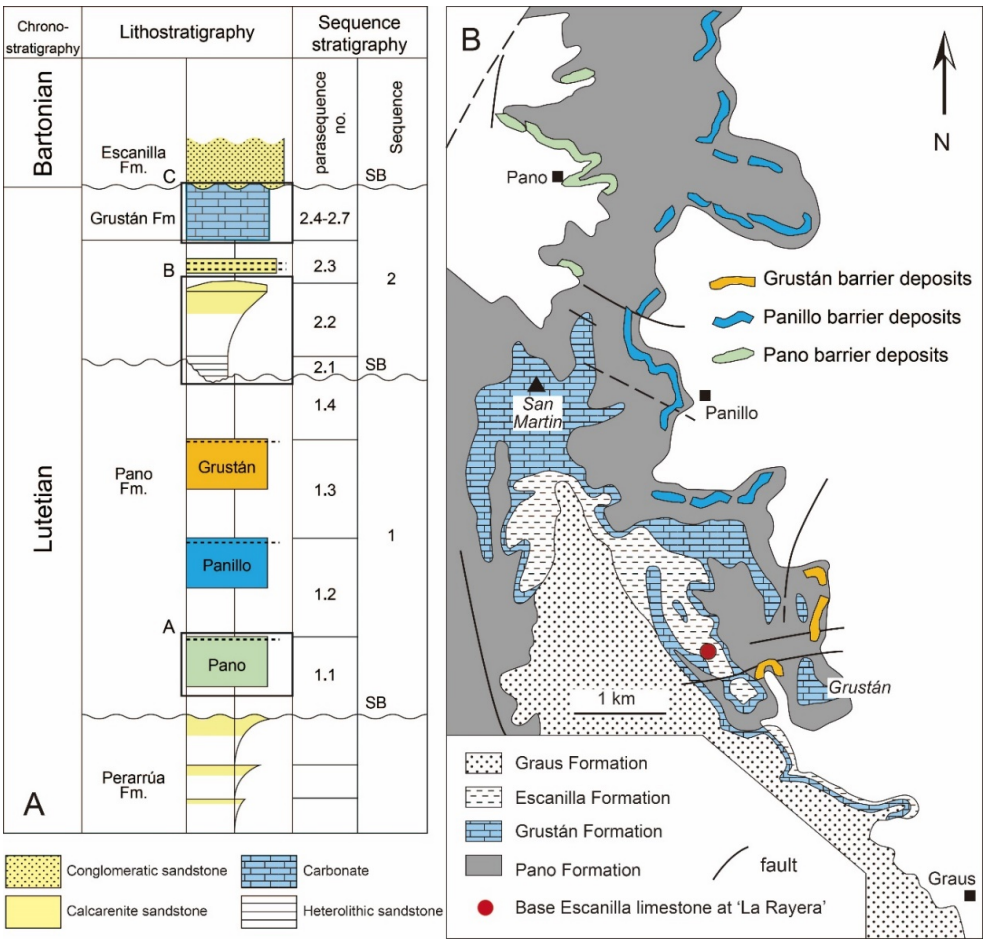

Figure 2.1: A - General stratigraphy of the Pano and Grustán formations, with sequence boundaries and parasequences. Modified after Donselaar (1996). B - Map of the Pano Formation between the villages of Grustán and Pano, showing the location of successive barrier deposits (modified from Donselaar and Nio (1982); and Donselaar (1996)).

2.1.4. Depositional Environment

The lower interval of Sequence 1 was deposited in a paralic clastic coastal zone, representing intertongued marine and continental environments influenced by waves, tides, and fluvial discharge [16]. The coastal barrier chains are superposed in a retrogradational fashion, first towards the east and then successively and clockwise rotating to the south, in tandem with the rotational development of the Mediano anticline [16]. The system comprised barrier islands or a large spit, with associated back-barrier lagoons and tidal inlets.

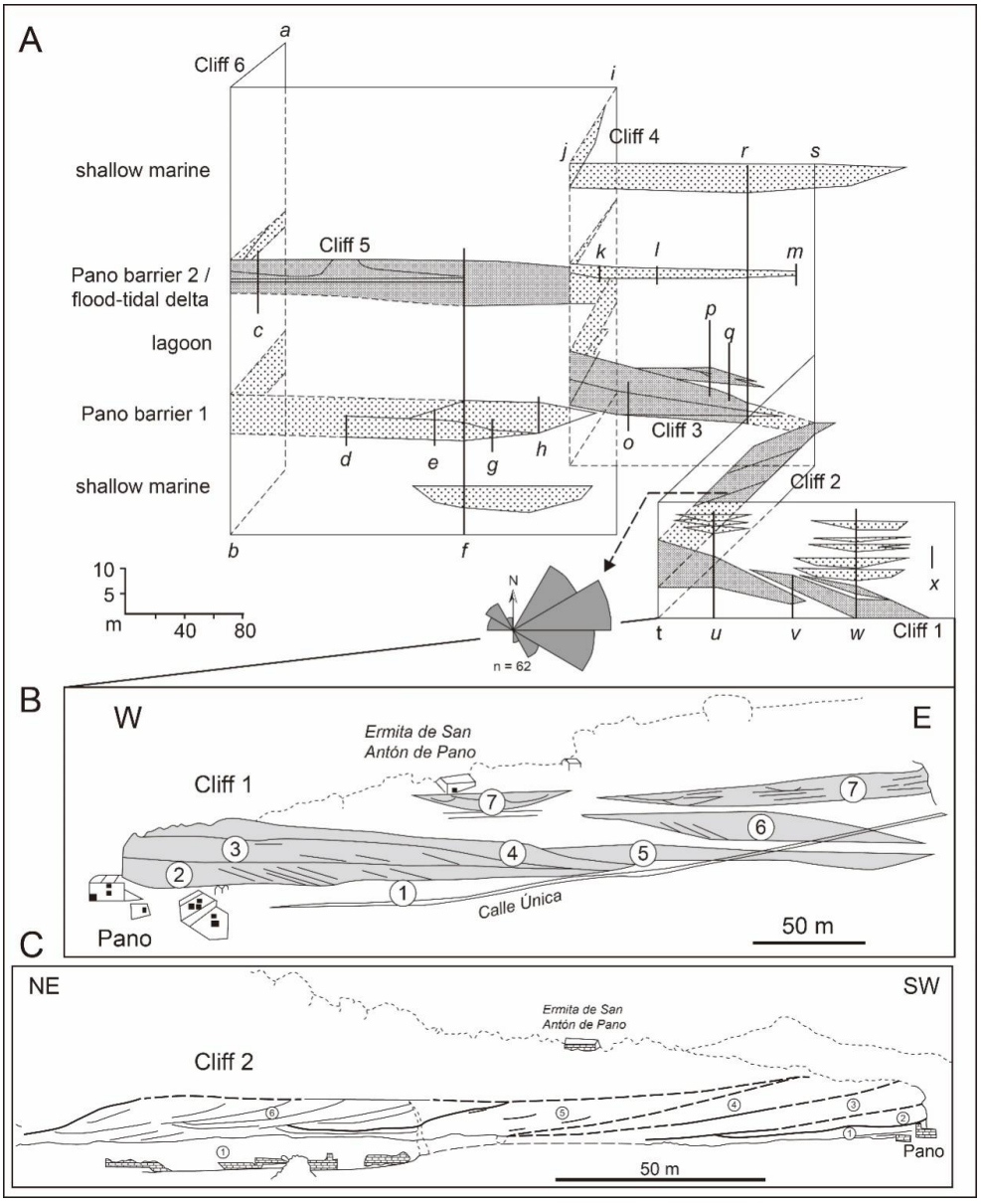

Figure 2.2: A - Overview of the Pano barrier and flood-tidal delta succession near the village of Pano showing a panel with six cliff faces and two stratigraphic intervals with barrier complex deposits (nr. 1 and 2). Pano barrier complex 1 is also exposed in a more southern location along the road from Pano to Lapenilla and Aldea de Puy de Cinca. The base is approximately 30 m below the Pano flood tidal delta. The flood tidal delta discussed here is exposed in cliffs 1 to 3; the associated barrier in cliffs 5 and 6 (not reported in Donselaar, 1996). The enlargements of W-E trending cliff face 1 (B) and NE-SW trending cliff face 2 (C) show large-scale architectural elements of the flood-tidal delta prograding in a seaward (SW) to landward (NE) direction; individual lobes are numbered. The palaeoflow directions are measured on cliff face 2. Details of Pano barrier complex 2 in cliff face 2 are illustrated in Fig. 3A and C; other details exposed in W-E trending cliff face 3 in Fig. 4B and D. See Fig. 1 for location reference. Modified after Donselaar (1996).

The transfer of sand from these spits or barriers led to the formation of flood-tidal deltas [16, 28]. The focus of this study, the flood-tidal delta near Pano village, is exceptionally well-exposed in 3D. It has a wedge-shaped geometry, thinning from 16 m in the west to 4 m in the east over a distance of 150 m, with a width of approximately 1 km [29, 16]. The succession begins with a coarsening-upward interval from bioturbated grey marl to hummocky cross-stratified (HCS) sandstones, interpreted as a progradational

lower shoreface [30, 23]. This is overlain by a thick composite sandstone body with large-scale (up to 15°) east-dipping inclined bedding surfaces, which separate five distinct flood-tidal delta units (Figure 2.3). The units exhibit sigmoidal foreset laminae and an east-west bimodal paleoflow. The tidal signature is confirmed by small-scale planar cross-stratified sets atop convex-up reactivation surfaces showing an opposite palaeocurrent direction [16].

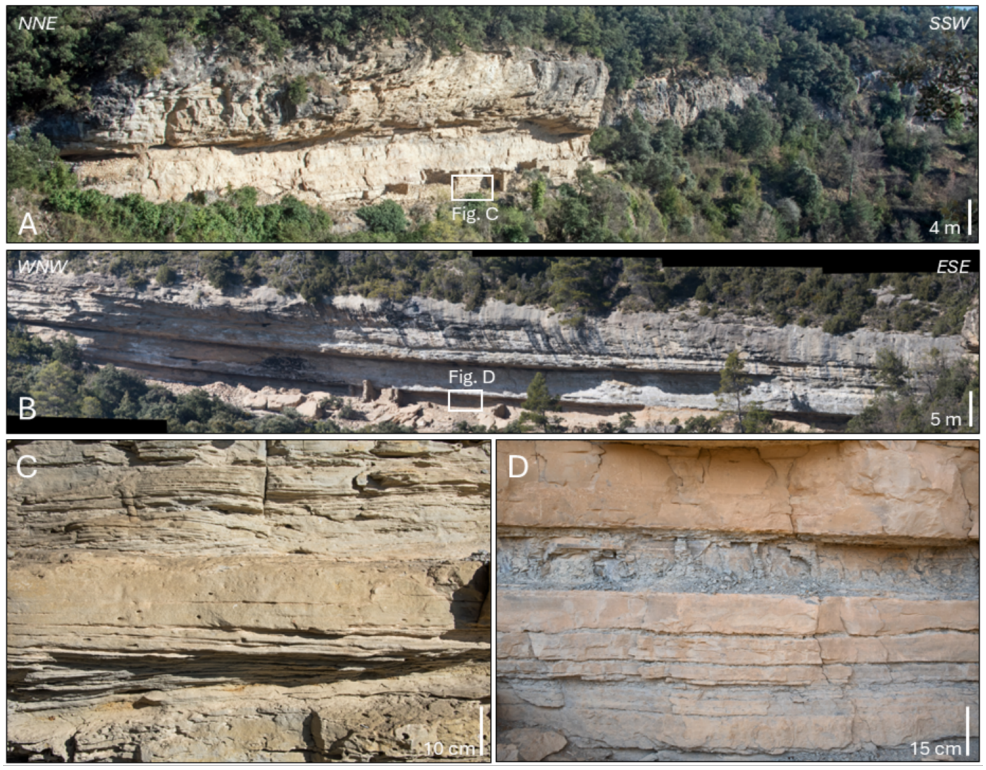

Figure 2.3: The Pano flood-tidal delta in cross sections. A – NNE to SSW cross-section obliquely to the direction of progradation (cliff face 2 of Fig. 2); note the large-scale inclined stratification. B – WNW to ESE cross-section of cliff face 3 (Fig. 2). C and D - Interval of hummocky and swaley cross-stratification generated by waves in the lower shoreface (C; cliff face 2, interval 1 at the location of the buildings on the NE side) and shoreface transition zone (D; cliff face 3, central part). It is eroded by the basal surface of the overlying flood-tidal delta complex.

Lens-shaped, tide-dominated feeder channels up to 4 m thick and 200 m wide are present. These trough cross-stratified sandstone units fine upwards and display a bimodal (E to NW) foreset dip direction, though within a single channel fill, one palaeocurrent direction is usually dominant [16]. This, along with the common occurrence of mud drapes, suggests a mesotidal setting and continual exchange of water between the open sea and the back-barrier lagoon [16, 31].

The flood-tidal delta complex is capped by a regionally extensive, up to 20 cm thick conglomeratic layer, interpreted as a transgressive lag formed during a relatively rapid relative sea-level rise (shoreline retrogradation) [16]. The overlying succession consists of several upward-coarsening sandstone intervals alternating with bioturbated marls and fine-grained sandstones, interpreted as an open marine shallow-water embayment, possibly related to the retrogradational stacking of more southeastward-located tidal delta deposits [16]. The detailed measured section of this embayment succession is provided in Appendix A.1.

The evolutionary model summarized above, characterized by retrogradation, clockwise rotation of barrier-lagoon systems, and the overarching tectonic control of the growing Mediano anticline, is synthesised in the palaeogeographical reconstruction presented in Figure 2.4. This sequential restoration vividly illustrates the southward and clockwise migration of the depocenters from the Pano (1) to the Panillo (2) and finally to the Grustán (3) barrier complexes. The reconstruction provides a visual summary of this

evolutionary model, depicting the southward and clockwise migration of the depocenters. It also highlights the role of the Mediano anticline, as interpreted from evidence such as sediment slumping off its flanks. Within this regional context, the well-exposed Pano flood-tidal delta represents a key component of the earliest phase of this evolving coastal system.

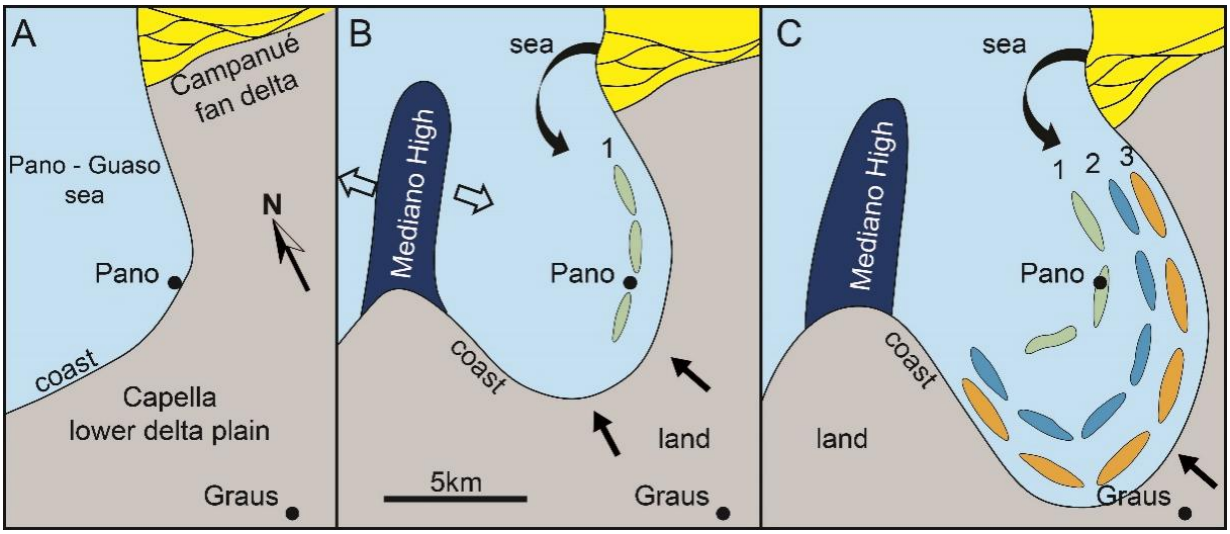

Figure 2.4: Palaeogeographical reconstruction and sequential development of the three barrier intervals in the Capella - Pano – Guaso Sequence starting before the onset of transgression in the area between the villages of Pano to Grustán. 1 = Pano barriers, 2 = Panillo barriers, 3 = Grustán barriers. Pano and Panillo barriers were drowned when the Grustán barriers developed. Open arrows indicate sediment slumping and collapse off the growing Mediano anticline. Closed arrows show the direction of sediment input. Modified after Donselaar and Nio (1982) and Donselaar (1996).

2.2. A Process-Architecture Model for Flood-Tidal Deltas

Flood-tidal deltas are complex sedimentary systems whose internal architecture is a direct consequence of tidal processes. This section synthesizes a unified model that deconstructs the delta into its fundamental architectural elements, explains their scale-dependent expression, and establishes a multi-directional framework for lobe interpretation. This model provides the essential theoretical foundation for analyzing the outcrops in the study area.

2.2.1. Architectural Elements and Their Genetic Processes

The flood-tidal delta system can be deconstructed into a set of genetically linked, three-dimensional architectural elements, each defined by a unique geometry, internal fabric, and a specific depositional process [32, 33]. The morphology of each element is a direct record of the dominant flow conditions that created it (Figure 2.5).

1. **Flood Ramp:** As the fundamental feeder element, the flood ramp is a landward-shallowing channel that slopes upward from the inlet throat. Its sharp, erosive base and dominance of large-scale, flood-oriented planar cross-bedding are a direct sedimentological response to the peak energy of landward-directed flood tidal currents [34]. This element represents the primary conduit for sediment delivery into the system [28].
2. **Flood Channel:** At the landward terminus of the flood ramp, the confined flow diverges into smaller, shallow distributary channels. These elements distribute sediment across the delta platform and are characterized by flood-dominated cross-stratification, often showing evidence of lateral migration. Their formation is governed by the deceleration and expansion of the flood jet after it exits the ramp [34].
3. **Ebb Shield:** This element defines the highest and most landward part of the delta, forming a topographic core composed of well-sorted sand. Its position and composition are a result of sediment bypass during peak flood flows, with only the finest sediments being deposited at this furthest point

of inundation. The ebb shield is often heavily bioturbated or capped by marsh deposits, indicating periods of stability. Critically, it acts as a baffle, diverting and shaping subsequent ebb-tidal currents, which gives the delta its characteristic horseshoe-like morphology [34].

4. **Ebb Spit:** These curvilinear sand ridges extend from the flanks of the ebb shield back toward the inlet. They are constructional features formed by ebb-current reworking of the delta's margins. Their internal structure exhibits ebb-oriented or bipolar cross-stratification, recording the bidirectional nature of the tidal regime and marking the lateral boundaries of the active delta [34].
5. **Spillover Lobe:** During particularly strong ebb tides, currents may breach the ebb shield or spits, depositing small, lobate sand bodies in the protected interior [34]. These elements record localized, event-driven sediment bypass and contribute significantly to the internal heterogeneity of the delta complex. They represent the episodic, high-energy reworking of the "sheltered" parts of the system [28].

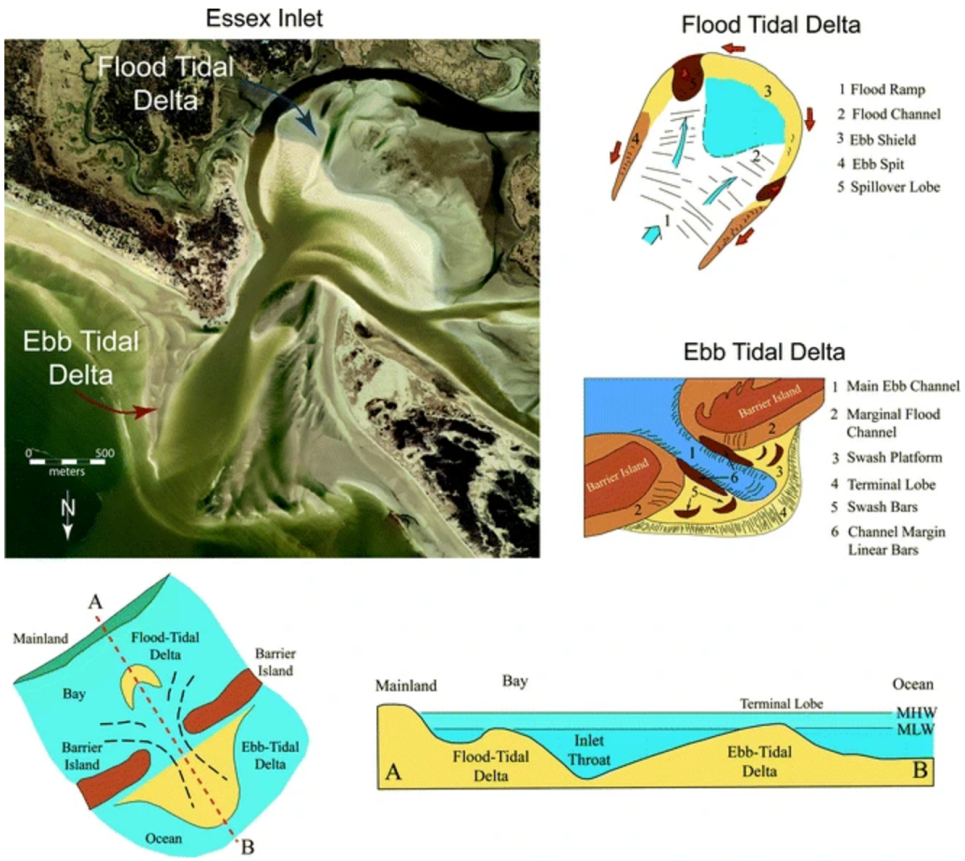

Figure 2.5: Ebb- and flood-tidal delta models (From Hayes (1979)). Aerial photograph of Essex Inlet, MA. Inlet cross-section model from FitzGerald (1996)

2.2.2. Delta Lobe Architecture in Multi-Directional Views

Delta lobes, the fundamental building blocks of a delta, exhibit dramatically different geometries depending on the observational perspective [35]. The classic model in Figure 2.6 provides a universal template for this analysis by decomposing the system into plan-view and cross-sectional views.

- **Plan View (Fig.2.6 A)** reveals the lobate form of the delta front, assembled from mouth bars and dissected by distributary channels.
- **Dip Section (Fig.2.6 B)**, parallel to sediment transport, showcases the diagnostic seaward-dipping clinoforms of the prograding delta front.
- **Strike Section (Fig.2.6 C)**, perpendicular to flow, captures the lenticular, mound-shaped geometry of individual lobes and the heterogeneity created by channel avulsion and lobe switching.

The multi-directional model established here provides the diagnostic framework for interpreting the study area's outcrops. We anticipate that the cliff-face exposures will capture a variety of lobe geometries, depending on their orientation relative to paleo-flow. Lobes exhibiting large-scale, basinward-dipping clinoforms will indicate a dip-oriented view, while those with lenticular, mound-shaped forms will represent a strike-oriented view. The vertical stacking of these differing lobe signatures will be the key physical evidence for reconstructing paleo-flow directions and documenting the process of lobe switching over time, directly linking the static outcrop record to the dynamic delta evolution.

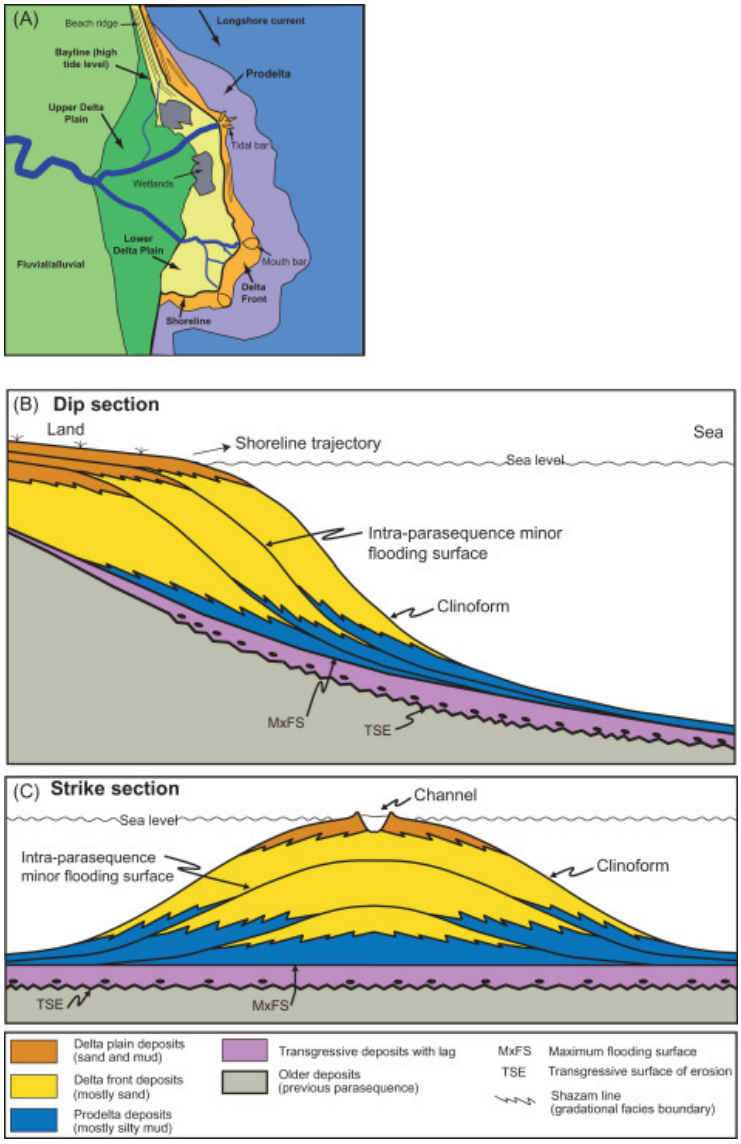

Figure 2.6: Classic depositional model of a prograding delta in plan-view and cross-sectional orientations. (A) Plan-view map of a delta showing various depositional environments, generalized from several modern and ancient examples. (B) Dip-oriented cross-section showing seaward-dipping clinoforms. (C) Strike-oriented cross-section showing bidirectional, mound-shaped clinoforms. Source: Modified from Gani and Bhattacharya (2005); as presented in Gani (2020).

2.2.3. Scale Dependency of Depositional Architecture and Cross-System Analogues

The expression and relative importance of these architectural elements are fundamentally scale-dependent, controlled by a hierarchy of processes from regional to local scales [37]. This hierarchical control not only dictates the internal heterogeneity of the flood-tidal delta but also provides a powerful

conceptual framework for understanding fluid flow in analogous subsurface systems like geological carbon storage.

1. **Macroscopic Scale (Delta Complex / Reservoir):**

   The very existence and overall size of the flood-tidal delta are controlled by regional external forcings. The tidal range and tidal prism are the primary determinants, with well-developed flood deltas being favored in microtidal settings [28]. The regional sediment supply and basin geometry provide the raw materials and the accommodation space for the delta to form.

   Cross-System Analogue:

   This scale is directly analogous to the reservoir scale in geological carbon storage. Here, the basin architecture and seal integrity control the overall containment of the CO_2 plume, just as the basin geometry and tidal regime control the existence and gross form of the tidal delta.

2. **At the Mesoscale (the scale of individual architectural elements):**

   The internal composition and geometry are governed by the dynamics of the tidal regime. The degree of tidal asymmetry controls the net sediment transport direction. The spring-neap tidal cycle imparts a rhythmicity to the deposition. Critically, the lateral migration and avulsion of flood channels and the formation of mud drapes and low-permeability laminations create a structured mosaic of flow properties that define the delta's internal heterogeneity [28].

   Cross-System Analogue:

   This scale corresponds to the scale of reservoir sedimentary architecture that controls capillary trapping. The low-permeability layers (e.g., mud drapes) deposited by these very tidal processes create the capillary heterogeneity that pins the CO_2 plume [11]. Thus, the mesoscale depositional processes are the genesis of the subsequent fluid flow baffles and barriers.

3. **At the Microscale (the scale of sedimentary structures within an element):**

   The specific internal fabric (e.g., the set thickness and foreset composition of cross-beds, the presence of mud drapes) is controlled by local, instantaneous hydraulics, including flow velocity and sediment grain size.

   Cross-System Analogue:

   At this scale, interfacial tension and pore geometry control the disconnection of the CO_2 phase into residual ganglia [7], a process directly analogous to the grain-scale hydraulics and particle interactions that control primary sediment deposition and the formation of specific sedimentary structures.

3

Datasets and Input Data

3.1. Geological Data

This study is grounded in the analysis of the Pano flood-tidal delta deposits, located in the Tremp-Graus Basin. The geological framework is defined by a hierarchical interpretation (L1–L4), established in Chapter 5 from a representative segment measuring 138 m in width and 24.8 m in height. This multi-scale approach systematically characterizes the heterogeneities present in the system, with the physical dimensions of the interpreted units at each level quantified as follows:

- **L1 (Macro-Architecture):** 12 m high, 138 m wide
- **L2 (Major Lobes & Barriers):** 2–12 m high, 20–138 m wide
- **L3 (Sub-lobes & Internal Heterogeneity):** 1–7 m high, 10–138 m wide
- **L4 (Finest Architectural Details):** 1–3 m high, 2–138 m wide

Among these, the L2 model is established as the primary focus for subsequent fluid diagnostics (Chapter 7). The dimensional range of its constituent units, specifically their decametre lateral extent, aligns with the definition of medium-scale heterogeneities. Investigating the fluid flow behaviour within this specific scale is paramount to understanding and predicting CO_2 plume migration and ultimate storage efficiency in analogous subsurface reservoirs.

3.2. Petrophysical Data and Property Assignment

3.2.1. Data Source and Subsurface Analogue

The Pano outcrop itself lacks subsurface well control or core data for direct petrophysical measurement. To overcome this limitation and create geologically realistic reservoir models, this study adopts a subsurface analogue approach. The chosen analogue is the Middle Jurassic (Bajocian) Etive Formation in Well 35/11-25A [1], situated in the Apodida prospect of the North Sea. This unit, developed between 3680 m and 3620 m, has been extensively studied and is recognized as a tide-influenced, flood-tidal delta complex. Its depositional setting and interpreted facies architecture provide a compelling and well-constrained analogue for the Pano system, ensuring that the subsequent property assignment is grounded in a real-world depositional environment.

The quantitative inputs are sourced from core measurements of this analogue formation (data courtesy Equinor ASA). The data reveal a clear facies-controlled property distribution: high-quality, thick-bedded sandstones exhibit porosities of 10–19% and permeabilities in the 12 mD range, while thinly bedded, silty intervals form low-permeability baffles with porosities as low as 3% and permeabilities around 0.02 mD. The highest reservoir quality is associated with inlet channel facies, where permeability can reach up to 200 mD.

3.2.2. Petrophysical Property Assignment

The transition from the qualitative geological framework established in Chapter 5 to a quantitative reservoir model required a systematic property assignment strategy that reconciles three key aspects:

[1] Subsurface analogue data from the 35/11-25A Wellbore (Equinor ASA, 2024), available at: https://factpages.sodir.no/en/wellbore/pageview/exploration/all/9284

(1) the facies-controlled property distribution from the analogue dataset, (2) the significant burial depth difference between the analogue (≈3650 m) and the Pano outcrop, and (3) the need to introduce geologically realistic heterogeneity while maintaining numerical stability for subsequent flow diagnostics. This strategy culminated in a comprehensive property lookup table (Table 3.1).

Based on the entire outcrop characterization, five distinct lithofacies groups were identified and populated with petrophysical properties following these principles: permeability in the x- and y-directions was set equal to reflect depositional homogeneity within the paleo-horizontal plane. In contrast, vertical (z-direction) permeability was defined as 20% of the horizontal permeability (k_v/k_h = 0.2) [38], consistent with compaction trends observed in analogous siliciclastic sequences.

The specific property assignment for each lithofacies group was determined as follows:

1. **Mudstone:** This lithofacies corresponds to thinly bedded silty layers in the analogue data, primarily distributed in the lower part of the outcrop succession. While the analogue suggests permeabilities as low as 0.02 mD, a minimum value of 1 mD was adopted to ensure numerical convergence in subsequent flow simulations.
2. **Shaly Sand:** Widely distributed along lobe margins and surrounding muddy interbeds in the outcrop, this facies was numerically correlated with the thick-bedded sand units from the analogue dataset. Permeability in x- and y-directions was set to 1–5 times the analogue value (10–60 mD), capturing its intermediate reservoir quality.
3. **Clean Sand:** As the main constituent of depositional lobes, this high-quality facies was matched to inlet channel sands in the analogue. Permeability was set to 0.5–3 times the maximum analogue value (100–600 mD).
4. **Shaly Sand + Clean Sand:** Applied to transitional lithologies slightly inferior to clean sand, this mixed facies was assigned properties intermediate between clean sand and shaly sand endmembers.
5. **Shaly Sand + Mudstone:** Representing transitional lithologies between shaly sand and mudstone, this facies was populated with properties geometrically averaged between these two endmembers.

Table 3.1: Summary of lithofacies groups and assigned petrophysical properties, based on subsurface analogue data from the 35/11-25A Wellbore (Equinor ASA).

Lithofacies Group	**Analogue Unit**	**Analogue ϕ (%)**	**ϕ (%)**	**Analogue $k_{x\&y}$ (mD)**	**$k_{x\&y}$ (mD)**	**k_v/k_h**
Mudstone	Thinly Bedded Silty Layers	3	7.5	0.02	1	0.2
Shaly Sand	Thick-bedded Sand Units	10–19	13.5	12	10–60	0.2
Clean Sand	Inlet Channel Sands	10–19	17.5	Up to 200	100–600	0.2
Shaly Sand + Clean Sand	Transitional Unit	n.d.	15.5	n.d.	100–300	0.2
Shaly Sand + Mudstone	Transitional Unit	n.d.	10.5	n.d.	1–10	0.2

The specific property values assigned to different model realizations are provided in the Appendix A.2.

4

Methodology

4.1. Overview of the Workflow

The methodology of this study follows a structured workflow designed to systematically investigate the impact of hierarchical geological heterogeneity on CO_2 storage performance. The process, summarized in Figure 4.1, progresses through four key phases: (1) Outcrop Interpretation, (2) Hierarchical Static Modeling, (3) Petrophysical Property Assignment, (4) Flow Diagnostics Analysis, and (5) Comparative Analysis and Synthesis.

The cornerstone of this approach is the hierarchical modeling strategy. Beginning with a simplistic, two-layer benchmark model (L1), geological complexity was progressively increased through a series of discrete steps. This involved incorporating major lobe elements and barriers (L2), subdividing these lobes into internal architectural units (L3), and finally introducing small-scale heterogeneity (L4). The specific methodology for this hierarchical static geological modeling is detailed in Section 4.3.

The subsequent flow diagnostics phase provided a suite of quantitative metrics to evaluate and compare the dynamic response across all four models (L1 to L4). Among these metrics, the Flow/Storage Capacity Ratio (F/V), whose formal definition is provided in Section 4.5.5, was of paramount importance for analyzing the temporal evolution of flow partitioning. The comprehensive flow diagnostics procedure, including the setup of boundary conditions, is elaborated in Section 4.5.

4.2. Outcrop Interpretation

The interpretation of the Pano outcrop was conducted within the LIME software environment (Figure 4.2), which served as the primary platform for the three-dimensional analysis of geological heterogeneities. The core of this stage was a systematic, hierarchical characterization of the outcrop, designed to deconstruct its architectural complexity across multiple scales.

This process involved a multi-tiered interpretation of heterogeneity, progressing from the largest architectural elements down to finer-scale features. A total of five distinct hierarchical levels were identified and digitally mapped. It is important to note that the finest scale (Hierarchy Level 5) was interpreted for contextual reference but was not incorporated into the subsequent reservoir modeling workflow due to computational constraints. The specific criteria, descriptive statistics, and spatial distributions for each interpreted hierarchical level are detailed in Section 5.

4.3. Hierarchical Static Geological Modeling

The hierarchical geological models were constructed within the **Rapid Reservoir Modelling (RRM)** software environment (Figure 4.3) [39]. RRM is an open-source research code designed for rapid geological model prototyping through its Sketch-Based Interface and Modelling (SBIM) approach. The core of its methodology is Surface-Based Geological Modelling (SBGM), where geological heterogeneities—such as stratigraphic surfaces, facies boundaries, and faults—are explicitly represented by three-dimensional surfaces. These surfaces are generated from two-dimensional sketches made in cross-section or map-view, and they interact based on a suite of geological operators (e.g., Remove Above, Preserve Between) to form watertight geological domains [39, 40]. This paradigm contrasts with traditional grid-centric methods,

as the model is defined by geological surfaces independent of an underlying grid, which is only generated later for visualization or flow computation [41, 39].

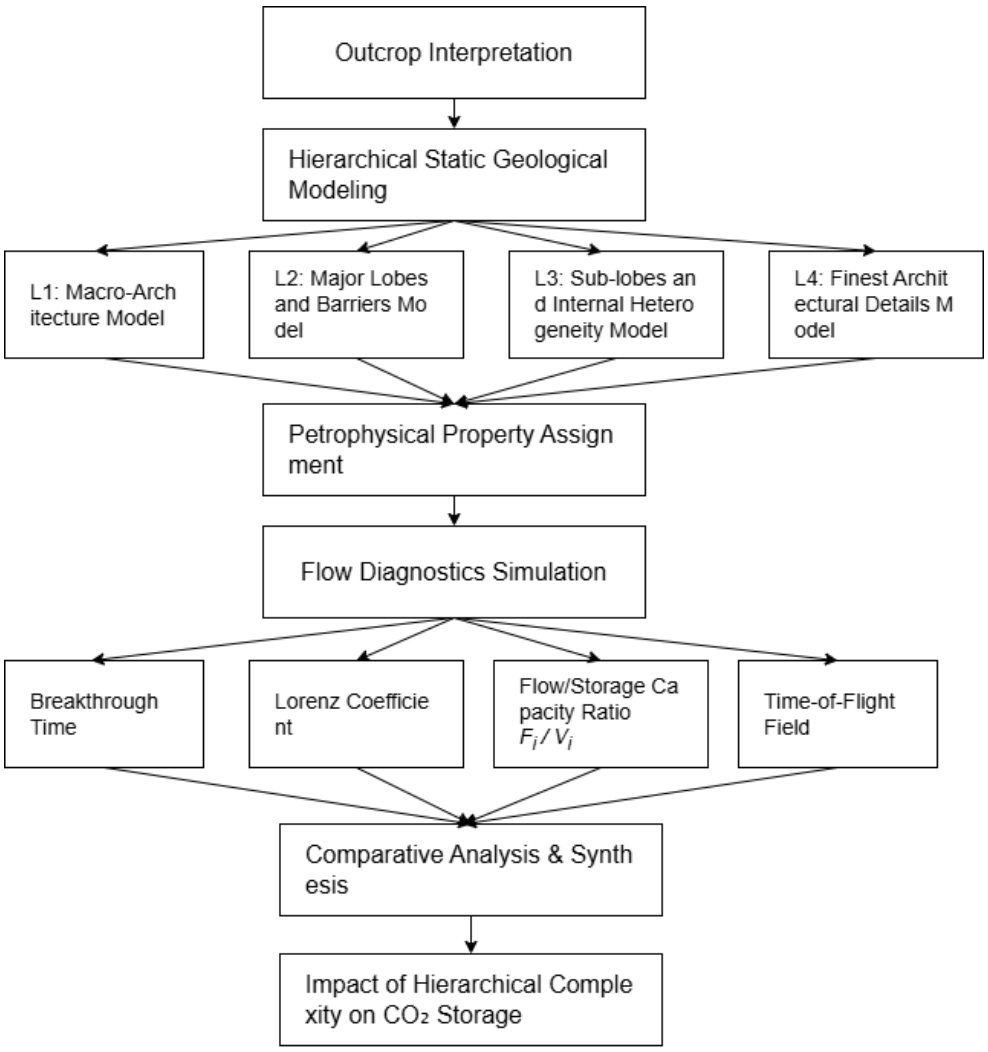

Figure 4.1: Integrated workflow for hierarchical geological modeling and flow diagnostics.

In the context of Carbon Capture and Storage (CCS), RRM's strengths are particularly well-suited to addressing key challenges arising from data sparsity and geological uncertainty at prospective storage sites. Its primary application lies in the rapid screening of multiple, equally plausible geological scenarios to evaluate the impact of sedimentological heterogeneity on CO_2 plume migration and stratigraphic trapping potential [42, 43]. For instance, Jackson et al. utilized RRM to efficiently construct 32 different scenario models for the Johansen Formation, systematically testing the impact of uncertainties in delta planform geometry, clinoform dip, and the distribution of carbonate concretions on CO_2 migration.

A critical feature for CCS applications is RRM's integration with computationally efficient **Flow Diagnostics (FD)** modules. This integration provides immediate quantitative feedback on CO_2 injectivity and plume migration patterns during the active injection phase [40]. Flow diagnostics, which solve a single-phase, steady-state pressure field, yield key metrics such as time-of-flight and pore volume injected at breakthrough. These metrics serve as powerful proxies for assessing how different geological heterogeneities act as conduits, baffles, or barriers to the migrating CO_2 plume [42, 39]. This combined RRM-FD approach enables geoscientists to quickly identify the most influential heterogeneities, thereby focusing subsequent, more time-consuming multiphase simulations on the critical scenarios [43].

The RRM software, including source code and executable versions, is publicly available at: `https:`

//bitbucket.org/rapidreservoirmodelling/rrm.

The initial step involved creating a model template with dimensions of 1380 m × 1380 m × 248 m, designed to encompass the full spatial extent of the Pano outcrop, with the assumption of an equal lateral extent in the x and y directions.

Subsequently, the digital interpretations of geological heterogeneities at different hierarchical levels, completed in LIME, were imported into RRM's E-W-oriented drafting panel. These interpretations served as direct templates, guiding the precise delineation and construction of the discrete heterogeneity units within the 3D grid.

Two specific aspects of the modeling process warrant explicit mention. First, during the model setup, the dimensions were inadvertently scaled by a factor of 10 in all directions (x, y, and z) compared to the original outcrop measurements. However, this uniform scaling does not affect the relative trends or qualitative conclusions drawn from the flow diagnostics results, as these metrics are primarily influenced by the internal architectural geometry and contrast in properties rather than the absolute dimensions. A detailed discussion on this matter is provided in Section 8.2.3.

Second, due to project time constraints, the heterogeneity was explicitly characterized and modeled only along the E-W direction. The N-S direction was not explicitly interpreted and was effectively represented as homogeneous in the current models. The implications of this assumption and the associated model limitations are critically evaluated in Section 8.2.1.

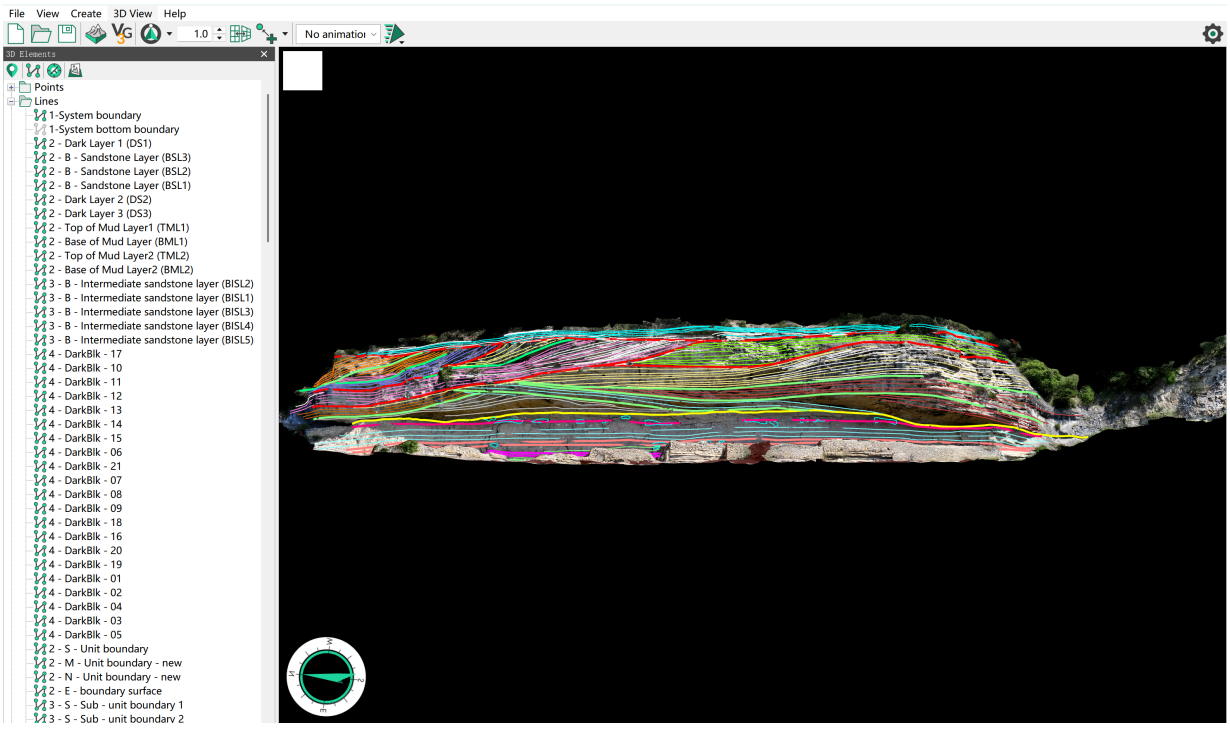

Figure 4.2: Digital interpretation of the Pano outcrop within the LIME software environment.

4.4. Petrophysical Property Assignment

The strategy for populating the hierarchical geological models with petrophysical properties was guided by the principle of establishing a consistent and geologically realistic link between lithofacies and flow characteristics. The core of this strategy involved developing a reference standard for property assignment based on the analyzed outcrop and its geological background analogue.

The detailed rationale behind the selection of specific porosity and permeability values for each lithofacies group, the adjustments made to account for differences in burial depth, and the overall property assignment strategy are discussed at length in Section 3.2.2. The resultant property lookup tables, which

summarize the final petrophysical values (porosity and permeability in the x, y, and z directions) assigned to each lithofacies unit within every model realization (L1 through L4), are compiled in Appendix A.2 .

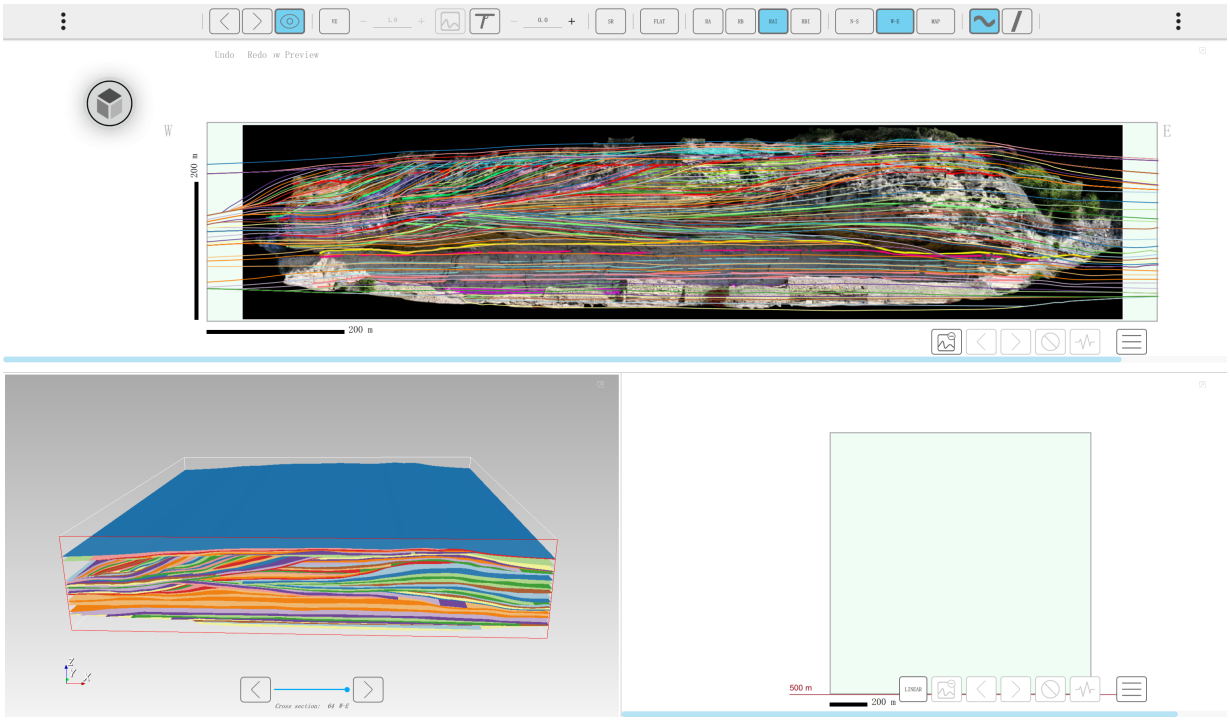

Figure 4.3: Construct the static model of the Pano outcrop within the RRM software environment.

4.5. Flow Diagnostics for CO_2 Storage Assessment

This study employs **Flow Diagnostics (FD)** to rapidly evaluate the impact of hierarchical geological heterogeneity on CO_2 migration and storage efficiency. FD is a suite of computationally efficient methods that solve a single-phase, steady-state pressure equation for a given well configuration to derive key metrics that proxy reservoir performance [44, 45]. While not simulating full multiphase physics, FD provides immediate, quantitative insights into connectivity, sweep efficiency, and stratigraphic baffling—critical factors during the CO_2 injection phase [42, 39]. The following subsections detail the specific metrics used, the simulation setup, and the hierarchical analysis methodology.

4.5.1. Flow Diagnostics Procedure

The flow diagnostics procedure was executed systematically across all hierarchical models (L1–L4) to capture their dynamic responses. The process began with models that had been populated with petrophysical properties, utilizing the grid dimensions specified in Section 6.2. After applying consistent boundary conditions, single-phase flow simulations were performed for each model.

To ensure a comparative analysis across both time and model complexity, a set of key time slices was selected for all models: 10 years, 100 years, and 1000 years after the start of injection. These time slices represent short-term, medium-term, and long-term plume behavior. Additionally, model-specific breakthrough times (the BT of L1 and L2) and the time when the recovery factor first reached 1.0 for each respective model were included. At these critical times, key simulation results, including time-of-flight and flux fields, were recorded.

These outputs form the basis for the subsequent analysis, where the methodologies detailed in the following subsections: Section 4.5.2 defines the theoretical metrics calculated, Section 4.5.3 outlines the boundary conditions for the single-phase flow simulations, Section 4.5.4 describes the methodology for analyzing results across the four model complexities (L1–L4), and Section 4.5.5 explains the techniques for dynamically tracking flow partitioning within specific geological units over time.

4.5.2. Flow Diagnostics Metrics and Theory

The core FD metrics utilized in this analysis are defined below. These metrics allow for a quantitative comparison of dynamic responses across the hierarchical model suite (L1–L4).

- **Time-of-Flight (TOF)**: The time $\tau(\mathbf{x})$ for a neutral tracer to travel from an injector to a location **x** within the reservoir, derived from the steady-state velocity field. TOF maps visually highlight preferential flow paths and connectivity between wells [46].
- **Pore Volume Injected at Breakthrough**: This measures the cumulative injected volume (in pore volumes) at the moment the tracer first arrives at a producer. It is a key indicator of stratigraphic baffling and storage efficiency; a higher PVI signifies greater plume retention within the reservoir volume and slower migration, which is desirable for storage security [42].
- **Flow Capacity-Storage Capacity (F-Φ) Analysis**: This classic method characterizes dynamic heterogeneity. The storage capacity Φ and flow capacity F are defined as functions of the cumulative volume fraction z, sorted by permeability in descending order:

$$\Phi(z) = \frac{\int_0^z \phi(\xi)\, d\xi}{\int_0^1 \phi(\xi)\, d\xi}, \quad F(z) = \frac{\int_0^z k(\xi)\, d\xi}{\int_0^1 k(\xi)\, d\xi} \tag{4.1}$$

  where ϕ is porosity and k is permeability. The **Lorenz Coefficient (Lc)**, calculated from the area between the F-Φ curve and the 1:1 line (perfect homogeneity), provides a single scalar quantifying the overall flow heterogeneity, ranging from 0 (homogeneous) to 1 (infinitely heterogeneous) [47].
- **Flow/Storage Capacity Ratio (F/V)**: To analyze flow partitioning at the scale of individual geological units, we define a ”micro-Lorenz” metric. For any geological unit i, the ratio is:

$$\left(\frac{F}{V}\right)_i = \frac{F_i}{V_i} \tag{4.2}$$

  where V_i is the unit's fraction of the total pore volume (static storage potential), and F_i is its fraction of the total injected tracer volume (dynamic flow contribution). A ratio of 1 indicates neutral behavior; >1 identifies a preferential flow pathway; <1 indicates a stagnant or bypassed zone.

  However, in practical application, this interpretation should be treated as a continuous spectrum rather than a set of rigid categories. For instance, a value of 0.97 may indicate a functionally neutral unit, as minor internal heterogeneities or numerical dispersion can cause slight deviations from the ideal. The metric is most powerful for identifying clear trends and significant contrasts (e.g., 0.5 vs. 1.5) between units, which robustly reveal the architecture's dominant control on flow partitioning.

4.5.3. Flow Diagnostics Setup

To ensure a consistent and comparable basis for evaluating the impact of geological heterogeneity on CO_2 storage, a fixed well configuration and pressure regime were applied to all static models (L1–L4) during the flow diagnostics.

The well locations and operational parameters are summarized in Table 4.1. One injector (INJ) and one producer (PRD) were positioned along the model's central axis to maximize the interaction of the CO_2 plume with the heterogeneous architecture. Both wells are completed as vertical wells perforated across the entire reservoir thickness (Figure 4.4).

The producer well in this setup functions as an ”offtake well”. Its primary role is not to produce CO_2 but to create a stable and managed pressure gradient across the model, preventing unrealistic pressure buildup near the injector and ensuring a physically representative diagnosis of flow connectivity and heterogeneity effects under active injection conditions.

Table 4.1: Well configuration and operational parameters for flow diagnostics.

Parameter	Unit	Injector (INJ)	Producer (PRD)
X Location	m	172.5	1207.5
Y Location	m	690	690
Perforation Top	m	0	0
Perforation Base	m	248	248
Bottom-Hole Pressure	bar	55	1

The bottom-hole injection pressure was determined based on a common field-derived gradient of 1 psi/ft [48] to approximate a realistic subsurface condition. The calculation is as follows:

$$P_{inj} = \text{Gradient} \times \text{Depth} = (1, \text{psi/ft}) \times (248, \text{m}) \tag{4.3}$$

Unit conversion is required for consistency:

$$248\text{m} \times 3.28084\text{ft/m} = 813.65\text{ft} \tag{4.4}$$

$$P_{inj} = 1\text{psi/ft} \times 813.65\text{ft} = 813.65\text{psi} \tag{4.5}$$

Converting to bar:

$$813.65\text{psi} \times 0.0689476\text{bar/psi} \approx 56.1\text{bar} \tag{4.6}$$

A conservative and rounded value of 55 bar was selected for the simulations. The production pressure was fixed at 1 bar (atmospheric pressure) in this setup to create a strong driving force for flow, thereby enabling a clear diagnosis of the connectivity and heterogeneity effects within the reservoir models. A discussion on the rationale and implications of this boundary condition choice is provided in Section 8.2.2. Simulations were run using the Reservoir Recovery Method (RRM) until a recovery factor of 1 was achieved.

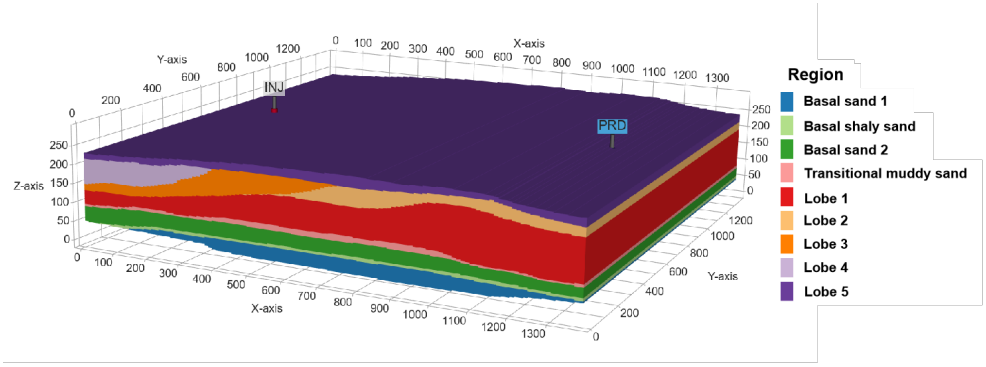

Figure 4.4: Location of the injector (INJ) and offtake (PRD) wells within the L2 reservoir model.

4.5.4. Analysis of Hierarchical Flow Diagnostics

To quantitatively deconvolve the contribution of heterogeneity at different scales to the overall flow behavior, a hierarchical analysis workflow was designed and implemented. The core of this methodology lies in distinguishing between model complexity and the scale of analysis.

- **Model Complexity:** Refers to the four static models (L1-L4) constructed, which contain an increasing number of geological units and architectural details.
- **Analysis Scale:** Refers to the specific level of geological architecture (e.g., the L2 ”lobes and barriers”) used as a template to aggregate and analyze the flow results.

The workflow, visualized in Figure 4.5, consists of two primary phases for any given analysis scale (e.g., L2):

1. **Flow Simulation:** The high-complexity models (e.g., L3 and L4) are simulated using the fixed well conditions described in Section 4.5.3. Their native, high-resolution results are stored.
2. **Results Aggregation:** The detailed flow results from Step 1 are not analyzed in their native complexity. Instead, they are mapped and aggregated according to the geological units defined in a simpler, coarser model that represents the target analysis scale. For instance, to investigate the flow behavior specifically at the L2 scale, the results from the L3 and L4 models are summed within the boundaries of the five major lobes and barriers defined in the L2 model.

4.5.5. Analysis of Dynamic Flow Partitioning

Flow partitioning refers to the dynamic process by which an injected fluid (CO_2) is unevenly distributed among different geological units within a reservoir, governed by contrasts in permeability, connectivity, and architectural arrangement. To quantify this phenomenon, the dynamic allocation of the injected CO_2 plume among geological units was analyzed using the **Flow/Storage Capacity Ratio (F/V)** defined in Equation 4.2. This metric was calculated for geological units across all models at the selected time slices detailed in Section 4.5.1.

This approach moves beyond qualitative plume observations, enabling a unit-by-unit comparison of how effectively different elements of the reservoir architecture capture and retain the injected fluid over time, directly revealing the evolution of preferential flow paths and bypassed zones.

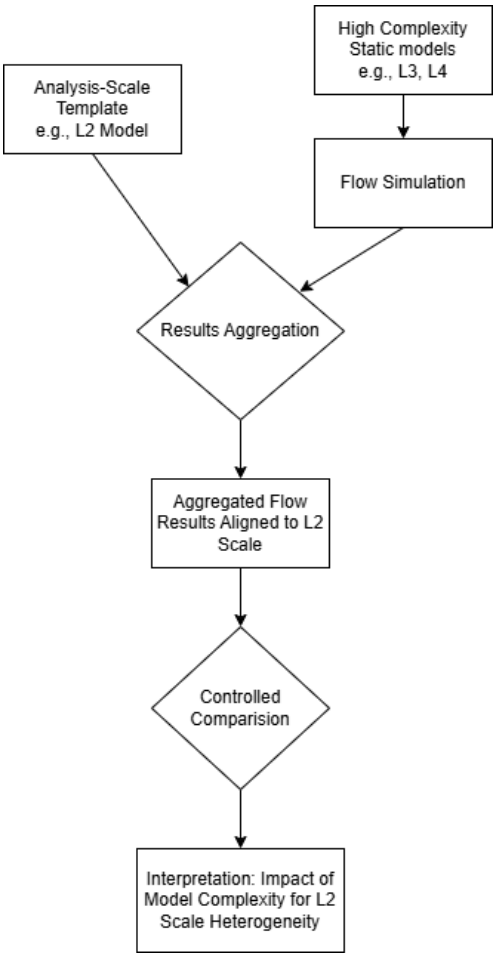

Figure 4.5: Workflow for the hierarchical analysis of flow diagnostics. Using the L2 Analysis Scale as an example.

5

Outcrop Interpretation

5.1. Basis for Outcrop Interpretation

This study utilized a high-resolution 3D digital outcrop panel provided by Associate Professor Joep Storms, which was constructed from UAV-derived photographs (Figure 5.1). This panel was imported into the LIME software to conduct geological interpretation and annotation directly on the outcrop model. The interpretation followed a fundamental principle of first identifying the largest-scale heterogeneities and then progressively refining the model by incorporating smaller-scale heterogeneous units. The final hierarchical interpretation results are detailed in Section 5.2. The identification and subdivision of these units were primarily based on the following principles:

1. **Geometry and Morphology:** The distinctive lobate form of sand bodies and their lateral termination styles (e.g., pinch-out versus abrupt erosional contacts) served as a primary criterion for defining heterogeneous units. This principle was crucial in delineating the major lobes at L2 and their internal subdivision into sublobes at L3.
2. **Bounding Surface Characterization:** Surfaces were classified as either erosional discontinuities or conformable interfaces based on the truncation and contact relationships of the strata. Unconformities identified in this manner were a critical basis for architectural division at both the L1 and L2 levels.
3. **Lithological Contrasts:** Vertical and lateral changes in lithology, particularly the occurrence of argillaceous sandstones or mudstones within sandstone bodies, were used to identify internal barriers. This approach was applied to define multiple shale-rich layers in the lower unit as distinct heterogeneities at L2 and L4.
4. **Stratigraphic and Paleo-depositional Relationships:** This principle was primarily applied at the more detailed L4 and L5 levels, guiding the interpretation of finer sandstone layers within lobes and sub-lobes. These layers provide evidence for the multi-phase formation and subsequent migration of the lobes over time.

5.2. Hierarchical Interpretation: L1 to L5

Using the LIME software, a hierarchical interpretation of the Pano flood-tidal delta outcrop was conducted. This process began by identifying the most prominent, large-scale heterogeneities and then systematically subdividing them into progressively smaller and more detailed heterogeneous units. This workflow ultimately led to the definition of five distinct hierarchical levels (L1 to L5), each capturing geological features at a specific scale.

5.2.1. L1: Macro-Architecture

L1 captures the fundamental architectural division of the outcrop into a two-part structure. The upper portion consists of dark-colored sandstone, which exhibits significant variations in morphology and weathering intensity from north to south, resulting in an irregular profile with both protruding and recessed features; its top is extensively covered by vegetation. The lower portion is defined by lightly colored, horizontally stratified sandstones with basal mud interbeds. A continuous, regionally traceable weathering horizon at the unconformity separating these two parts serves as the key baseline for defining the L1 heterogeneity (Figure 5.2).

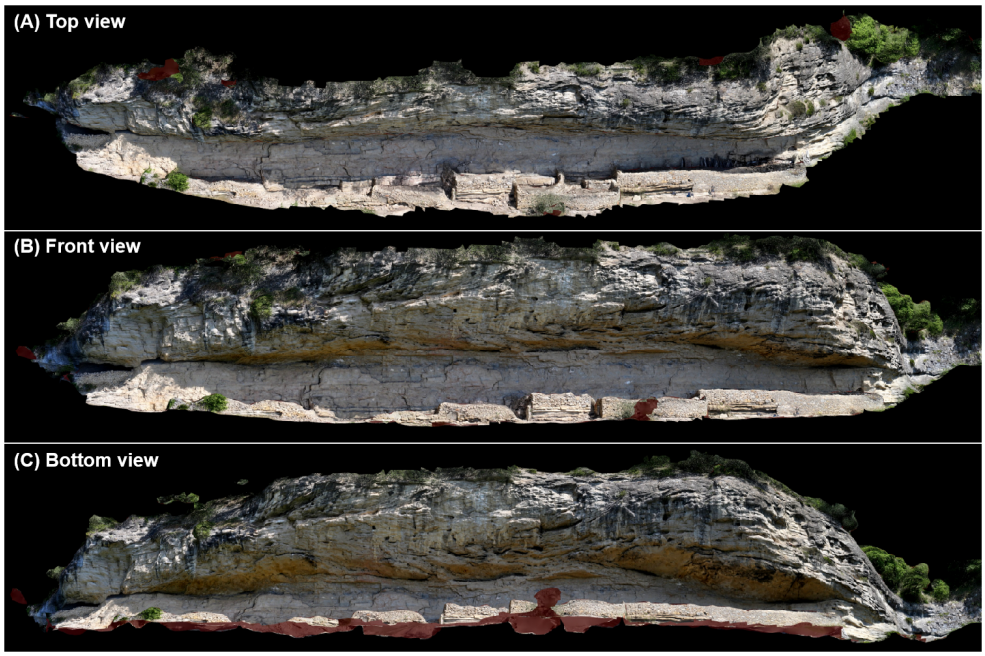

Figure 5.1: 3D model visualization of the Pano flood-tidal delta outcrop: (A) top view, (B) front view, (C) bottom view.

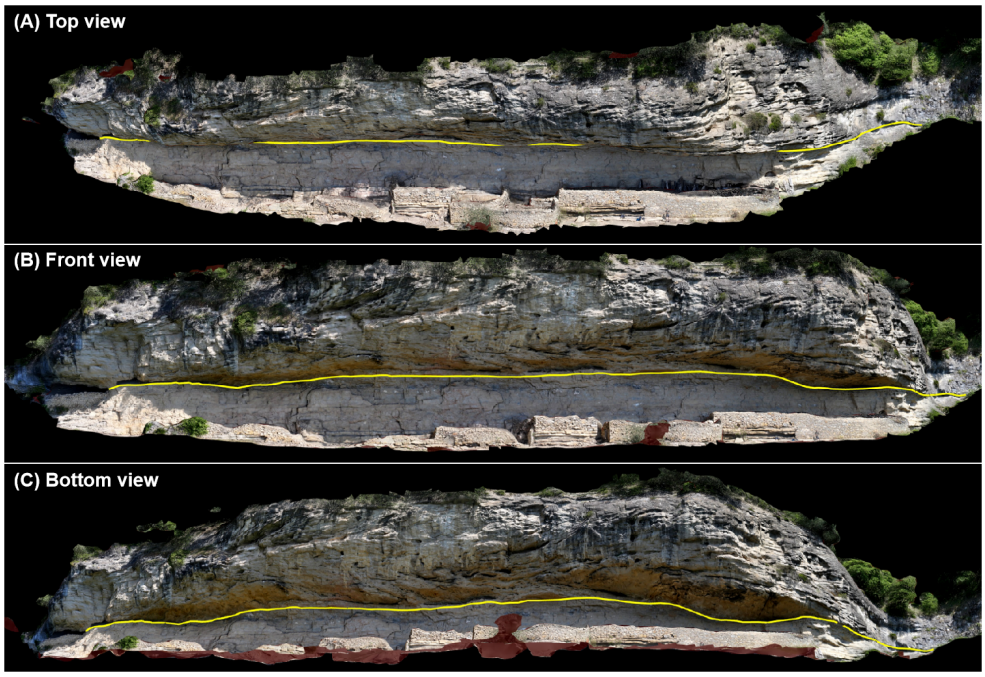

Figure 5.2: Outcrop interpretation at heterogeneity level L1: (A) top view, (B) front view, (C) bottom view.

5.2.2. L2: Major Lobes and Barriers

L2 delineates a more refined architectural framework by subdividing the major L1 units. Within the upper part, five discrete lobes are identified, which exhibit erosional and unconformable contacts alongside variations in paleo-depositional orientation, indicating a complex history of multi-phase deposition. In the lower unit, five distinct, color-defined mudstone layers are recognized as internal barriers (Figure 5.3). This level resolves the connectivity between these sub-units and captures key variations in their thickness and lateral extent.

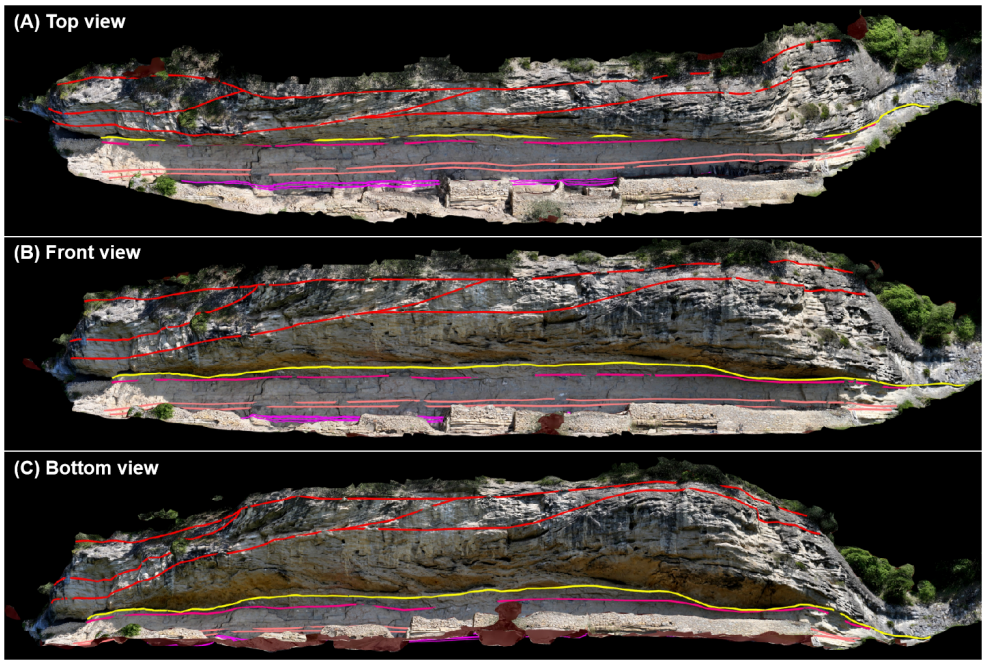

Figure 5.3: Outcrop interpretation at heterogeneity level L2: (A) top view, (B) front view, (C) bottom view. Different colors denote interpreted layers.

5.2.3. L3: Sub-lobes and Internal Heterogeneity

L3 delivers a finer-scale interpretation by subdividing the L2 architectural elements. In the upper unit, the oldest, basal lobe is subdivided into five sub-lobes based on variations in depositional orientation, color, thickness, and shale content. Furthermore, the two northern lobes are also resolved into multiple internal sub-lobes. In the lower unit, four sub-parallel sandstone layers are incorporated (Figure 5.4).

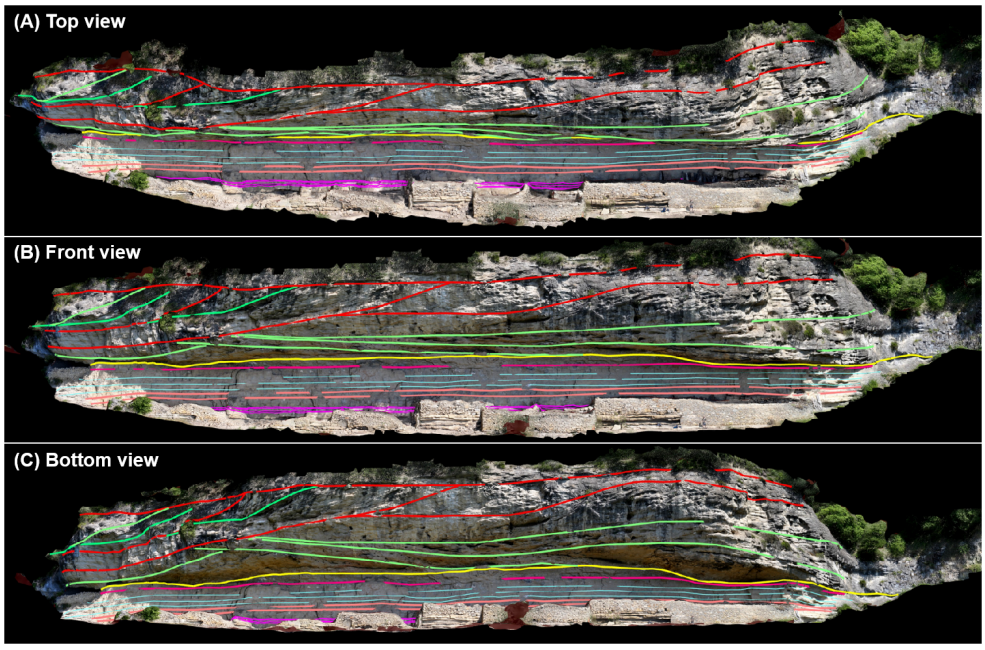

Figure 5.4: Outcrop interpretation at heterogeneity level L3: (A) top view, (B) front view, (C) bottom view. Different colors denote interpreted layers.

5.2.4. L4: Finest Architectural Details

L4 delineates the most detailed heterogeneity framework within the architecture established by L1-L3. In the upper unit, all sandstone layers within lobes and sub-lobes are individually characterized. Variations in their orientation, thickness, and contacts are critical for predicting post-injection fluid flow behavior. Sedimentologically, these layers record the progradation and multiple avulsions of lobe fronts, reflecting the interplay between sea-level dynamics and sediment supply over time. In the lower unit, thinner sandstone layers adjacent to and within the basal mudstone are incorporated (Figure 5.5).

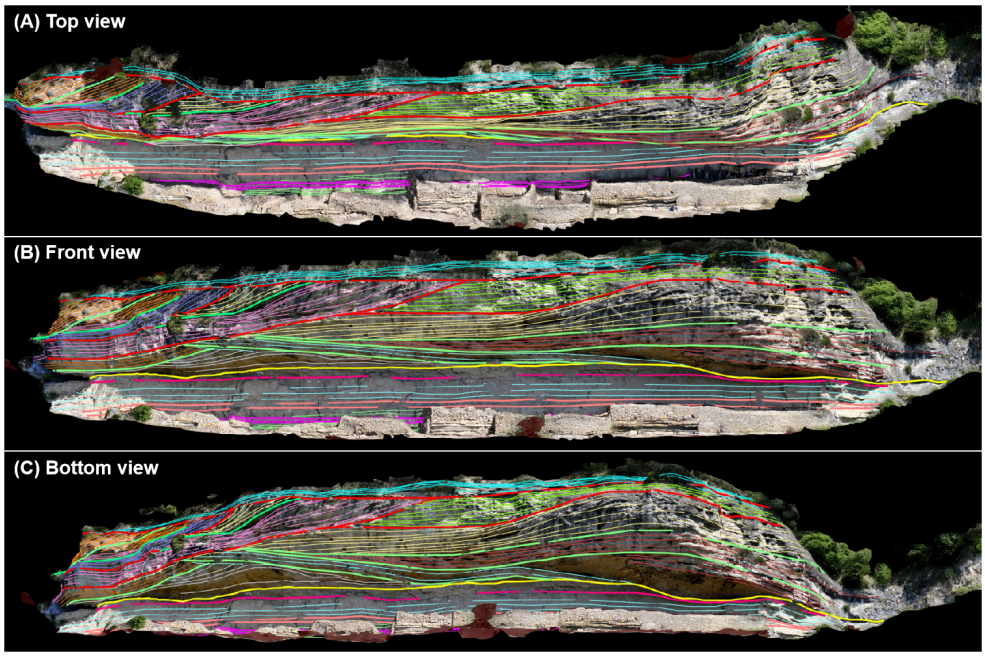

Figure 5.5: Outcrop interpretation at heterogeneity level L4: (A) top view, (B) front view, (C) bottom view. Different colors denote interpreted layers.

5.2.5. L5: Reference-Only

The L5 level was established to define the practical resolution limit of the current study and to document the full spectrum of observable heterogeneities. It augments the L4 model with additional, finer-scale details, such as subtle intra-sandstone layers and patchy, dark-colored features in the lower unit (Figure 5.6). Although these details are beyond the scope of the present modeling and simulation work, L5 plays a critical role as a conceptual bridge. It anchors our hierarchical interpretation to the finest observable scale, offering a reference for future investigations into the impact of small- to medium-scale heterogeneities.

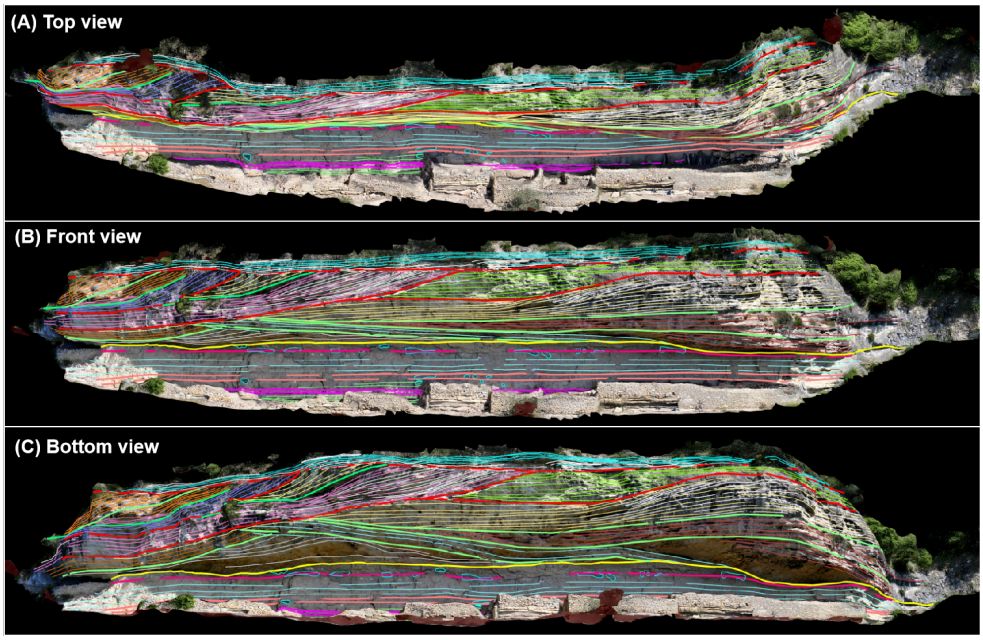

Figure 5.6: Outcrop interpretation at heterogeneity level L5: (A) top view, (B) front view, (C) bottom view. Different colors denote interpreted layers.

6

Static Model

This chapter presents the suite of three-dimensional static reservoir models that form the basis for the subsequent flow diagnostics. Following the workflow established in the Methodology (Chapter 4), four distinct models were constructed, representing a progressive increase in geological complexity from the macro-architectural L1 model to the highly detailed L4 model.

All models were built within a consistent volumetric domain measuring 1380 m (X) by 1380 m (Y) by 248 m (Z). It is noted that this domain represents a **tenfold** increase in the lateral and vertical dimensions compared to the original outcrop. Critically, this uniform geometric scaling has a negligible impact on the comparative results of the fluid diagnostics, which are the focus of this study. The flow behavior depends primarily on the internal architecture and the contrasts in petrophysical properties between geological units, both of which were preserved proportionally. Therefore, the conclusions regarding the relative impact of different heterogeneity levels (L1-L4) on CO_2 plume migration remain robust and entirely valid. A supplementary discussion on the invariance of flow diagnostics under proportional scaling is provided in Section 8.2.3.

6.1. Hierarchical Static Models: L1 to L4

6.1.1. L1 Model

The L1 model, corresponding to the Macro-Architecture level defined in Chapter 5, establishes the most fundamental, large-scale heterogeneity within the outcrop. This coarse model is constructed as a simple two-layer system, comprising lower basal sands and upper overlying lobes. The system is relatively homogeneous at this scale, with the basal sands and overlying lobes occupying 34% and 66% of the total model volume, respectively (Figure 6.1).

Serving as the foundational framework for all subsequent models, the L1 model defines the bounding geometry and volumetric proportions within which all higher-resolution architectural elements (L2–L4) are embedded and refined.

6.1.2. L2 Model

The L2 model refines the L1 framework by incorporating the major lobes and barriers, as interpreted in Chapter 5. The static model comprises five distinct lobes in the upper unit and a single, continuous mudstone interbed in the lower unit, all separated by an unconformable weathering horizon (Figure 6.2).

During the model construction process, one particularly thin mudstone interbed identified in the outcrop interpretation was omitted at this level. This decision was made to maintain a relatively uniform scale of heterogeneous bodies within the L2 model, ensuring a clear representation of its primary architectural elements.

The volumetric proportions of the constituent units are as follows: the five upper lobes constitute 35.2%, 7.6%, 9.0%, 6.2%, and 8.3% of the total volume, respectively. The lower unit is divided into two basal sand layers (10.9% and 15.3%), the key mudstone interbed (3.1%), and the unconformable transition zone (4.4%) (Figure 6.3).

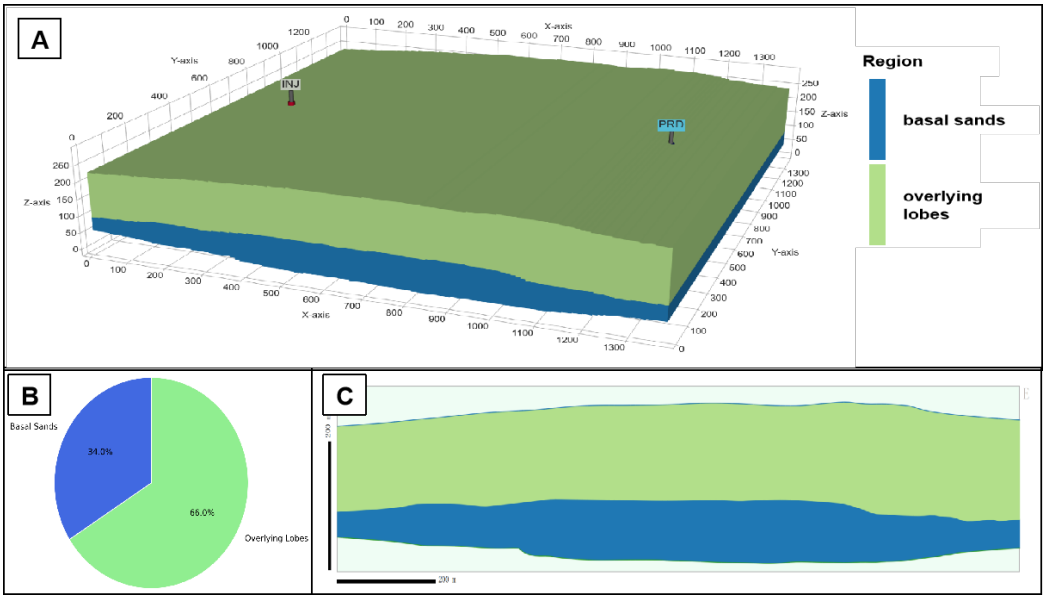

Figure 6.1: Static model characterization of L1: (A) 3D visualization of the geological model, (B) volumetric proportion of each heterogeneous unit, and (C) a stratigraphic slice through the W-E oriented transect.

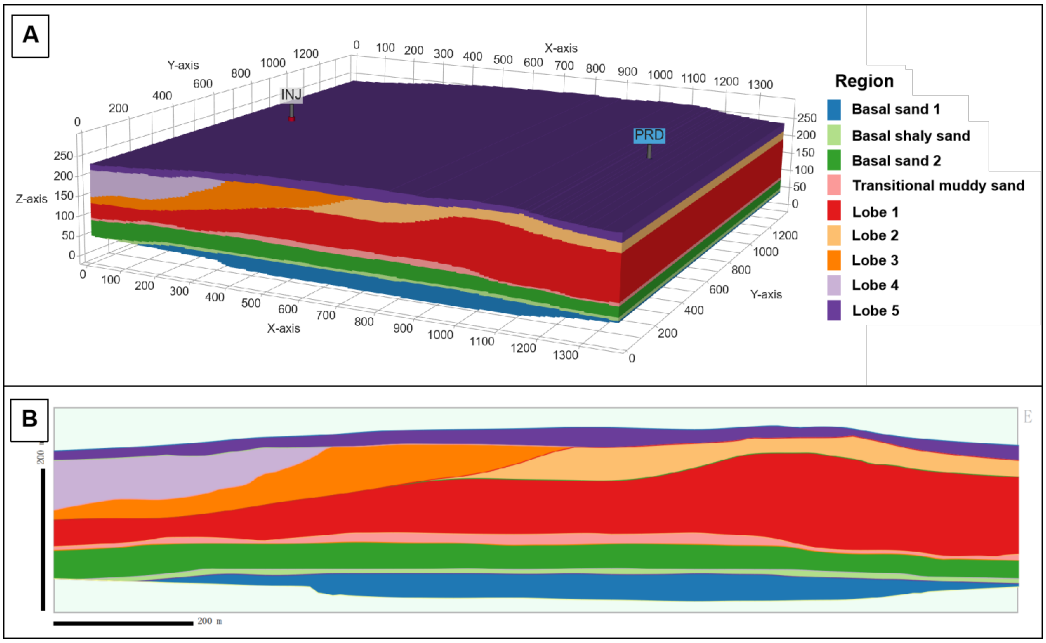

Figure 6.2: Static model characterization of L2: (A) 3D visualization of the geological model, (B) a stratigraphic slice through the W-E oriented transect.

6.1.3. L3 Model

The L3 model introduces a higher level of detail by subdividing the five major L2 lobes into genetically distinct sub-lobes based on sedimentological characteristics (Figure 6.4). For instance, Lobe 1 is partitioned to reflect its internal depositional evolution, progressing from basal, silt-rich sands through a composite lithofacies assemblage of the main depositional phase, to the cleaner, congruent-laminated sands of the late depositional stage.

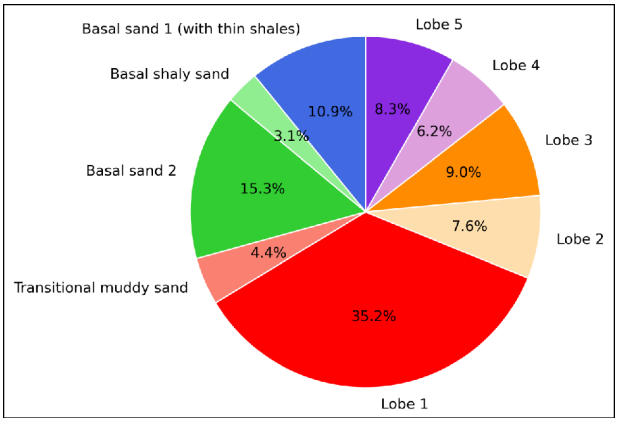

Figure 6.3: Volumetric proportion of each heterogeneous unit of L2.

Additionally, the lower unit is refined with the incorporation of thinner, more numerous mudstone interbeds. Following this subdivision, the congruent-laminated sub-lobe within Lobe 1, representing the late-stage deposits, constitutes the largest individual sub-unit with a relative volume of 13.5%. The remaining sub-lobes across the model exhibit a more uniform distribution in their volumetric contributions, as detailed in Figure 6.5.

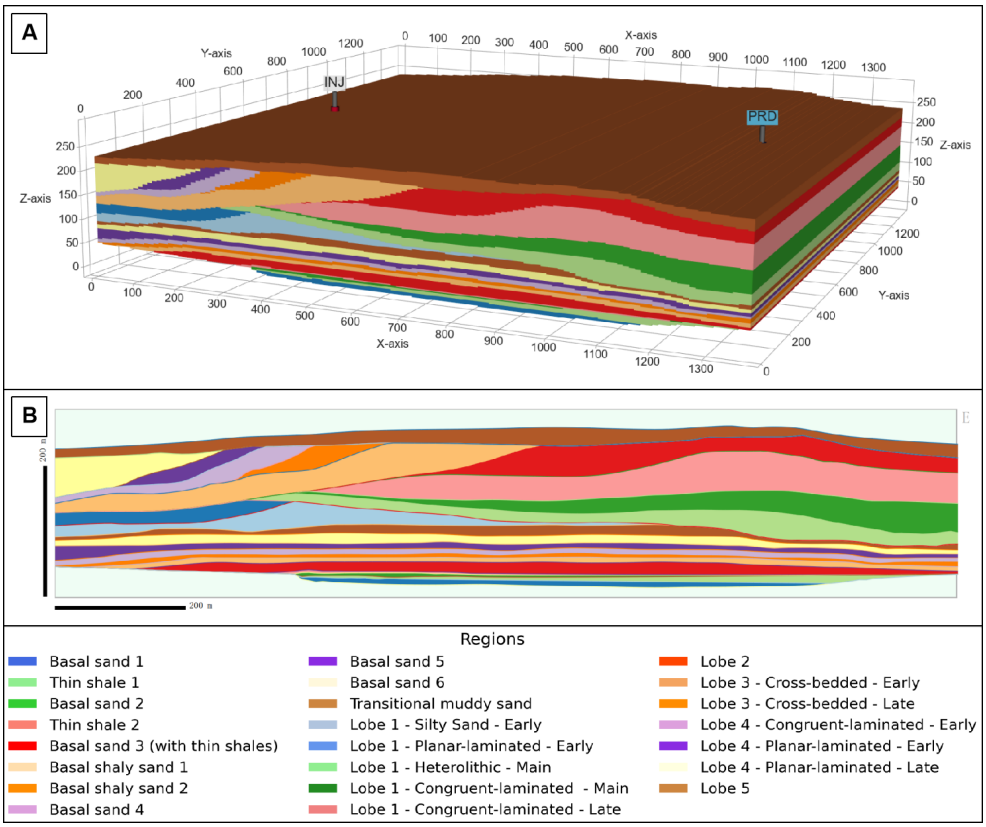

Figure 6.4: Static model characterization of L3: (A) 3D visualization of the geological model, (B) a stratigraphic slice through the W-E oriented transect.

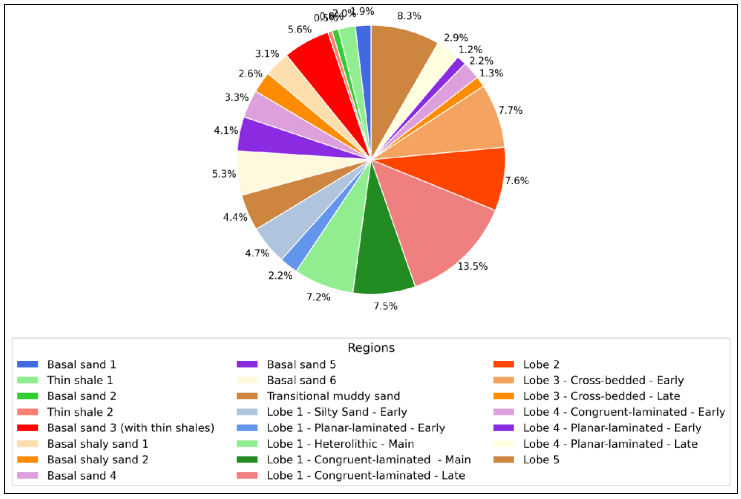

Figure 6.5: Volumetric proportion of each heterogeneous unit of L3.

6.1.4. L4 Model

The L4 model represents the highest tier of heterogeneity delineated in this study, corresponding to the Finest Architectural Details defined in Chapter 5. This model aims to capture the full spectrum of small-scale sandstone layers and subtle architectural elements observed in the outcrop. As the most geologically complex realization, it comprises approximately 100 layers. Given the high number of layers, the individual volume percentages and a detailed legend are not presented here but are encapsulated in the comprehensive model visualization (Figure 6.6).

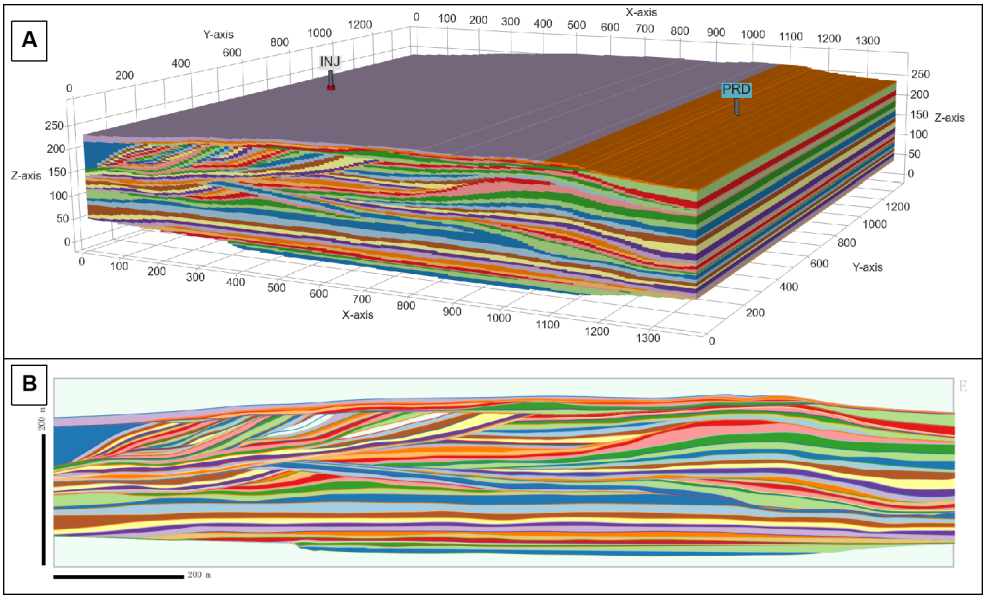

Figure 6.6: Static model characterization of L4: (A) 3D visualization of the geological model, (B) a stratigraphic slice through the W-E oriented transect.

6.2. Grid Resolution and Convergence Analysis

The geological models in this study span a wide spectrum of complexity, from the simple, two-layer architecture of L1 to the highly detailed, 100-layer system of L4. To represent these models in numerical simulations, the grid must be sufficiently refined to resolve the defining geological features and accurately capture the underlying physical flow processes. However, a trade-off exists: as grid resolution increases, so does the computational cost. Therefore, a convergence analysis was performed before the full suite of

fluid diagnostics to determine a grid resolution that provides a balance between numerical accuracy and computational efficiency.

A simplified, two-layer benchmark model was established for this analysis, with parameters summarized in Table 6.1. The model was simulated across a range of uniformly spaced Cartesian grids, from a coarse $21 \times 21 \times 21$ grid to a fine $161 \times 161 \times 161$ grid. Key performance metrics, including breakthrough time, Lorenz coefficient, and recovery factor at 1 PVI (Pore Volume Injected), were tracked and are presented in Table 6.2.

Table 6.1: Parameters for the grid sensitivity benchmark model.

Parameter	Value
Model Size (X $\times$ Y $\times$ Z) (m)	2802 $\times$ 2000 $\times$ 490
Wells	1 Injector (100 MPa), 1 Producer (80 MPa)
Upper Unit Permeability k_{xy}/k_z (mD)	600 / 100
Lower Unit Permeability k_{xy}/k_z (mD)	80 / 10
Upper Unit Porosity	29%
Lower Unit Porosity	20%

Table 6.2: Grid convergence analysis for the benchmark model.

Resolution	Breakthrough (yrs)	Yrs @1 PVI	Lorenz Coefficient	Recovery @1 PVI
$21 \times 21 \times 21$	2.63	17.8	0.662	47.7%
$61 \times 61 \times 61$	2.41	17.0	0.696	44.8%
$121 \times 121 \times 121$	2.29	16.8	0.706	43.9%
$161 \times 161 \times 161$	2.28	16.8	0.706	43.9%

The results demonstrate a clear trend towards convergence. As shown in Table 6.2, the breakthrough time and recovery factor stabilize beyond the $121 \times 121 \times 121$ resolution, with negligible changes observed at the finest grid. The Lorenz coefficient, a measure of dynamic heterogeneity, also plateaus, indicating that the flow patterns are adequately captured. This convergence is visually confirmed in the recovery versus PVI and recovery versus time plots (Figures 6.7 and 6.8), where the curves for the 121^3 and 161^3 grids are nearly indistinguishable.

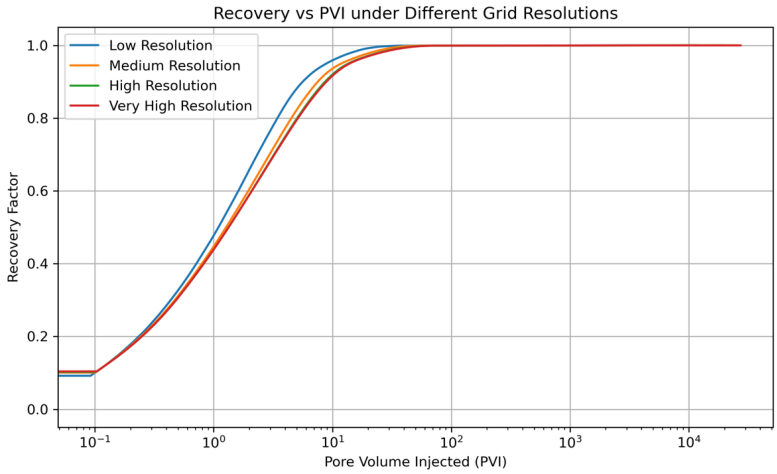

Figure 6.7: The effect of grid resolution on displacement efficiency vs. pore volume injected (PVI)

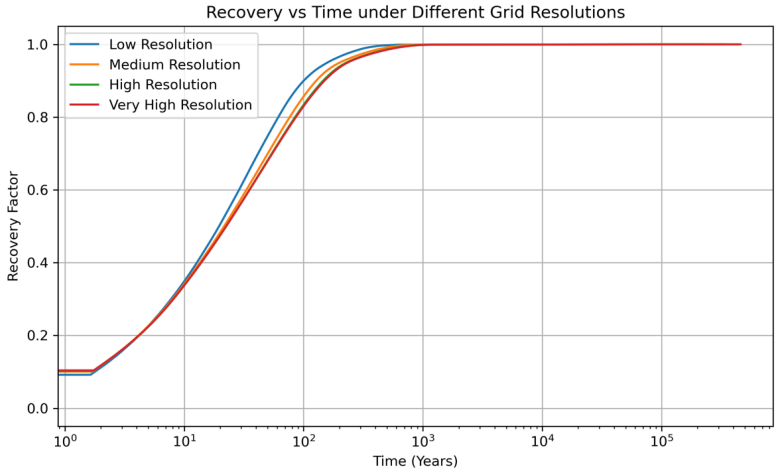

Figure 6.8: The effect of grid resolution on displacement efficiency vs. time (years)

The grid convergence analysis indicated that key metrics began to stabilize at a resolution of 121^3, as detailed in Table 6.2. Therefore, this resolution was adopted as the baseline for the extensive suite of L1–L4 model simulations to ensure computational feasibility. It is acknowledged, however, that the sufficient resolution for capturing all relevant physical processes in the most complex architectures remained an open question. A dedicated discussion on the potential influence of grid sensitivity on the final results is provided in Section 8.2.4.

7

Flow Diagnostics

7.1. Overview of Flow Behaviors Across Hierarchical Models

Following the workflow of static model construction, property assignment, and flow diagnostics established in Chapter 4, simulations were successfully conducted for all four hierarchical models (L1–L4). The comprehensive results are archived in Appendix A.3.

The Lorenz coefficient, a key metric of dynamic heterogeneity, exhibits a clear monotonic increase from 0.393 in the simple, two-layer Model 1 (L1) to 0.507 in the highly complex, 104-unit Model 4 (L4). This trend is visually reinforced by the flow-storage capacity ($F - \phi$) curves (Figure 7.1): the curve for Model 4 deviates more significantly from the 45-degree line of perfect homogeneity and arcs more strongly toward the upper-left corner compared to its simpler counterparts. This pattern signifies that as the model complexity increases, a progressively smaller volume of the pore space accounts for a disproportionately larger share of the flow, indicating a stronger flow anisotropy and the dominance of a few, well-connected high-permeability conduits.

Concurrently, the breakthrough time shows a marked decrease, falling from 22.26 years in Model 1 to just 8.48 years in Model 4 (Figure 7.2). This earlier breakthrough provides direct dynamic evidence that the injected fluid finds and preferentially travels through these efficient flow pathways more rapidly in the more geologically complex models.

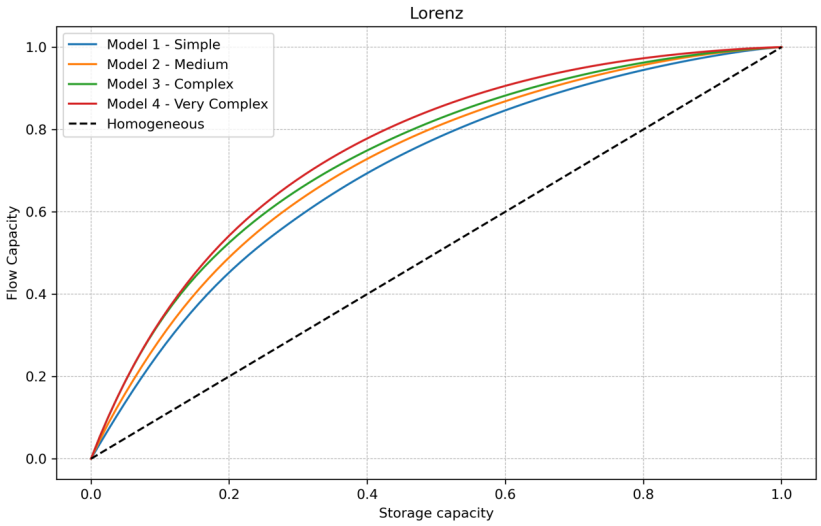

Figure 7.1: Lorenz curves for all model realizations.

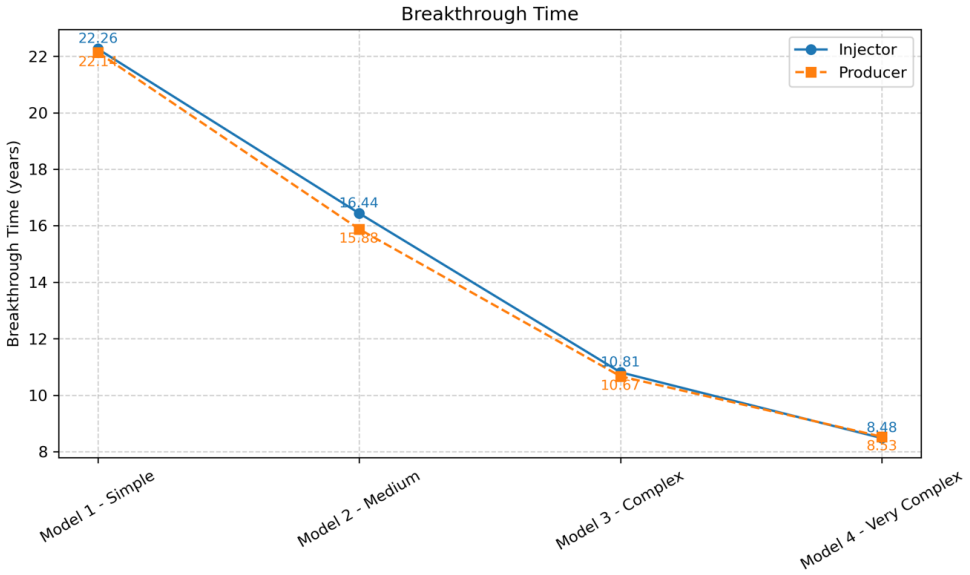

Figure 7.2: Breakthrough time comparison for the four geological models.

The evolution of recovery factor with injected pore volume (PVI) further elucidates the impact of heterogeneity (Figure 7.3). At 1 PVI, a significant divergence in recovery is observed, decreasing systematically with model complexity: 70.6% (L1), 66.9% (L2), 64.5% (L3), and 61.7% (L4). This highlights that geological complexity exerts its strongest control during the initial, advection-dominated displacement phase, where high-permeability conduits dictate flow efficiency.

While the difference between models narrows considerably by 6 PVI (L1: 99.7%, L2: 98.8%, L3: 98.1%, L4: 95.3%), this apparent convergence in our single-phase results requires careful interpretation. It indicates that the impact of heterogeneity on the final swept volume may diminish over extreme time scales, with all models asymptotically approaching 100% recovery. However, this theoretical endpoint is critically misleading for CO_2 storage assessment. In reality, CO_2 displaces brine through multiphase flow, where capillary trapping, relative permeability effects, and gravity segregation make 100% brine displacement physically impossible. These multiphase processes would be profoundly influenced by the very heterogeneities smoothed over in simpler models, likely amplifying the performance gap in terms of trapping efficiency and plume distribution.

Consequently, a geological model that oversimplifies the geometry produces a dangerously inaccurate forecast. It overpredicts early to mid-term injectivity and plume migration rates, while completely failing to capture the heterogeneous trapping dynamics that govern long-term storage security. The impractical timescale required for a full sweep in a complex system further underscores that oversimplification matters profoundly, as it misrepresents both the dynamic behavior and ultimate fate of the CO_2 plume.

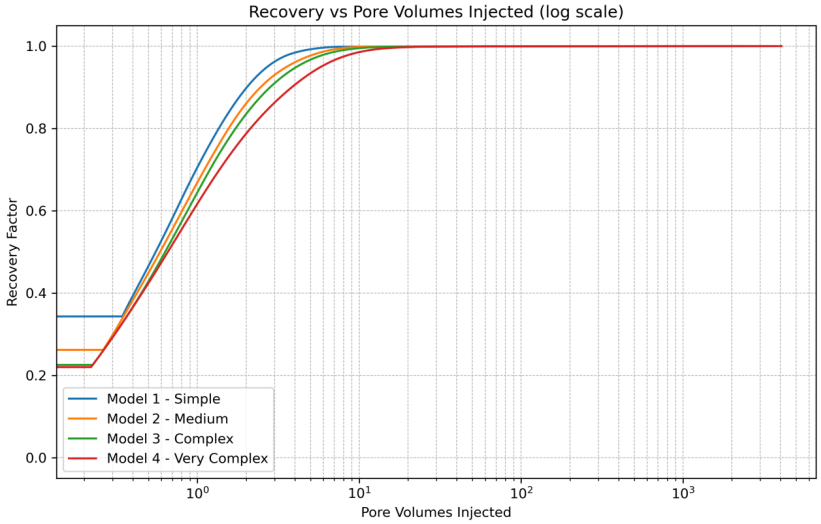

Figure 7.3: Displacement efficiency versus pore volume injected (PVI) for all model realizations.

This exceptionally long tail is mirrored in the recovery factor versus time plot (Figure 7.4). While all models exhibit rapid breakthrough and reach 99% recovery within the first year, the final 1% of the defending fluid requires an additional 343 to 346 years to be produced, irrespective of the model's architectural complexity.

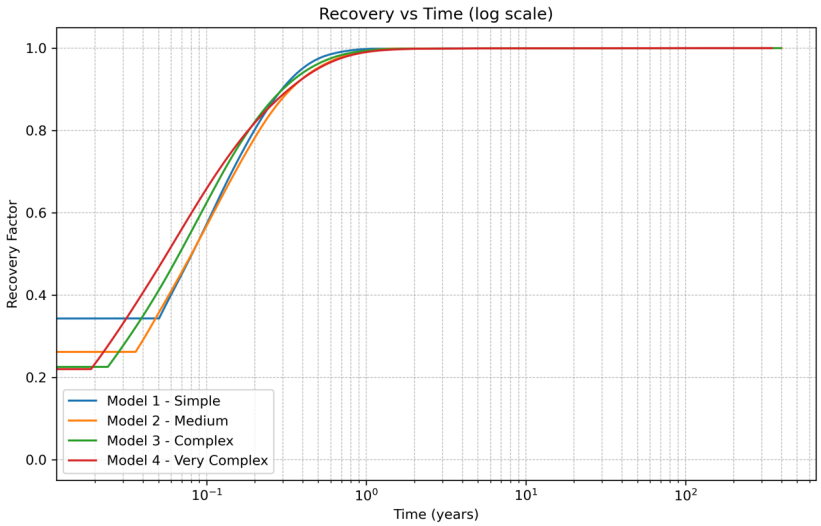

Figure 7.4: Displacement efficiency versus time for the four geological models.

7.2. Flow Partitioning[1] at the Macro-Architectural Scale: L1 Analysis

This section deconstructs the flow results by aggregating all dynamic data into the two fundamental architectural units defined in the L1 model: the Upper Unit and the Lower Unit. This analysis reveals the first-order control of the large-scale geological structure on CO_2 migration.

[1] For a detailed definition of "flow partitioning", see Section 4.5.5.

Figure 7.5 illustrates the evolution of the Flow/Storage Capacity Ratio (F/V), defined in section 4.5.5 for both units across all models at the fixed time slices of 10, 100, 1000 years, and at the first model's breakthrough time (22.26 years).

At the 10-year mark, a profound disparity is evident. The Upper Unit in all models exhibits an F/V ratio significantly greater than 1, confirming its role as the dominant preferential flow pathway from the very beginning of injection. In contrast, the Lower Unit displays a ratio much less than 1, signifying that it is largely bypassed. Furthermore, the internal architecture already exerts a measurable influence: the F/V ratio is highest in the most complex Model 4 (1.38) and Model 2 (1.36), and lowest in the simplest Model 1 (1.24). This suggests that the presence of interconnected, high-permeability conduits within the Upper Unit of the complex models enables even more efficient capture of the early injected volume.

At the breakthrough time, the F/V ratio for the Upper Unit remains high, underscoring that the breakthrough is fundamentally caused by the rapid channeling of CO_2 through this high-efficiency zone. The hierarchy among models remains, but the F/V values for the Upper Unit in Models 1, 2, and 4 begin to decline (to 1.21, 1.35, and 1.37, respectively), while Model 3 remains constant at 1.32.

By 100 years, the trend persists, but the F/V ratio for the Upper Unit begins a gradual decline as the unit becomes more fully saturated. Concurrently, the ratio for the Lower Unit shows an increase, suggesting the onset of filling. The F/V ratios for the Upper Unit continue to decrease as it becomes more fully saturated. Meanwhile, the Lower Unit experiences a substantial increase in its F/V ratio, with Model 3's value jumping from 0.34 to 0.81.

Finally, by 1000 years, a late-stage equilibration process is observed. The F/V ratios for both units in all models converge towards the neutral value of 1. This indicates that, over geological timescales, the injected fluid eventually redistributes itself more proportionally across the entire pore volume.

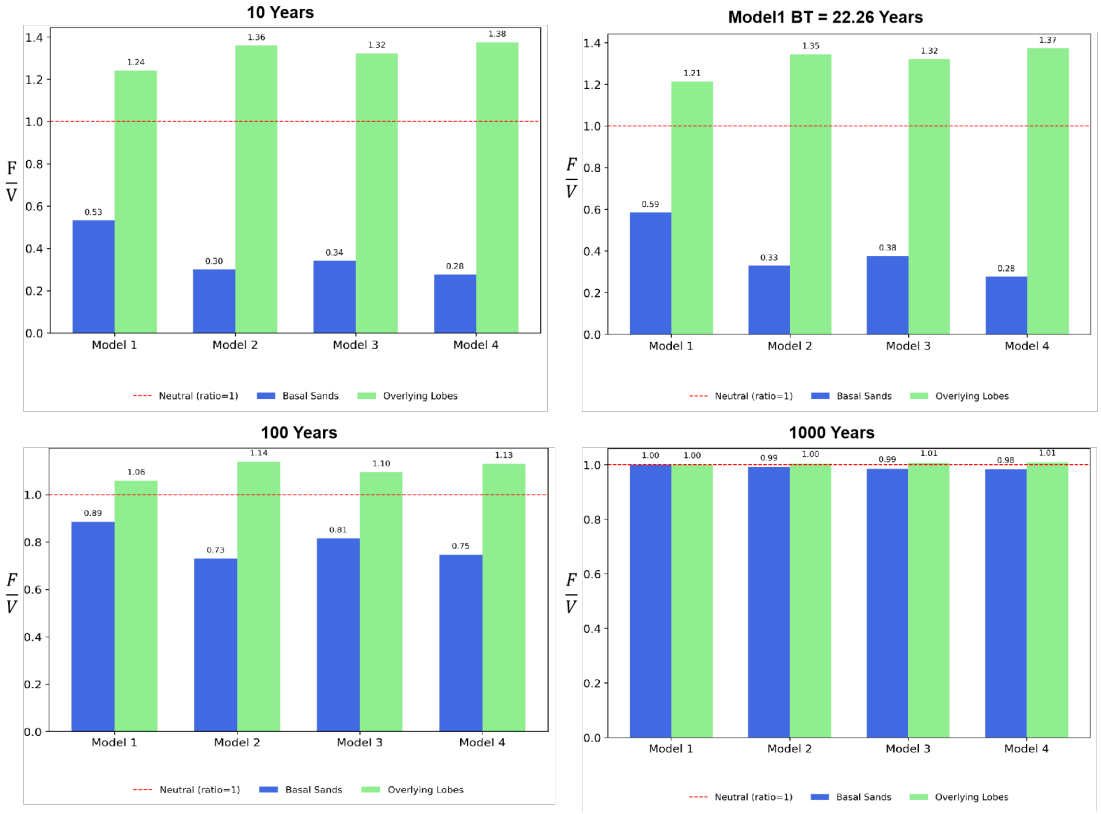

Figure 7.5: F/V Distribution at L1 Scale. Comparison across Model 1-4 at 10, 22.26, 100, and 1000 years.

7.3. Flow Partitioning at the Medium Scale: L2 Analysis

7.3.1. 10 Years

At the 10-year mark, Figure 7.6 reveals a clear and complex hierarchy of flow efficiency among the lobes, which evolves with model complexity.

In Model L2, a simple dichotomy exists: Lobe 4 (3.69) and Lobe 3 (3.25) act as the dominant superhighways, with their F/V values far exceeding 1. This indicates that in the absence of finer-scale heterogeneities, the flow is captured by a few, highly efficient pathways.

In Model L3, the introduction of sub-lobe architecture modulates this pattern. While Lobes 3 and 4 remain highly efficient (3.01, 3.03), Lobe 2 emerges as a significant, albeit less efficient, contributor (1.24). This suggests that the internal subdivision of lobes in L3 creates new, viable flow paths within Lobe 2, effectively "activating" it and distributing the flow more broadly across the upper unit compared to L2.

In Model L4, with the finest architectural details, the flow is distributed most broadly. Lobes 3 and 4 remain the most efficient (2.74, 2.91), but their dominance is slightly reduced. Lobes 2 and 5 are now both active pathways (1.34, 1.30). Most notably, Lobe 1 (0.77), though still a net bypassed zone, shows higher activity than the lower unit's barriers. This demonstrates that increasing complexity creates a more continuous spectrum of flow efficiency.

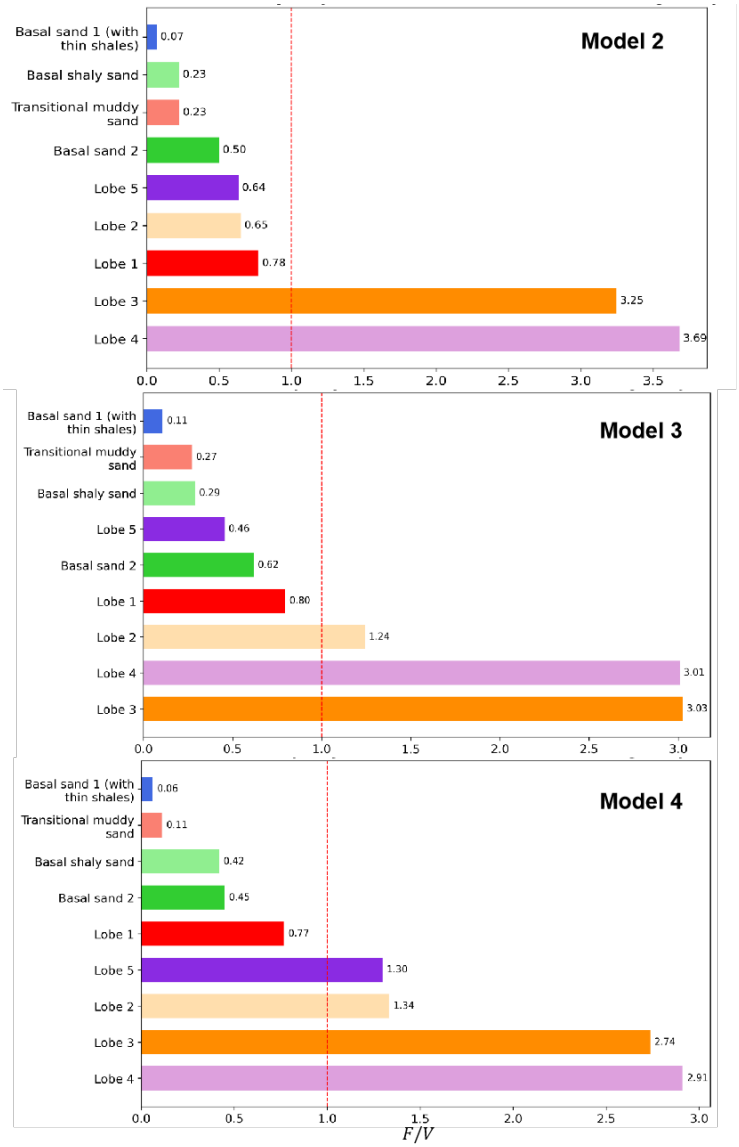

Figure 7.6: F/V Distribution at L2 Scale. Comparison across Model 2-4 at 10 years.

7.3.2. Breakthrough Time

At the breakthrough time (16.44 years), the flow partitioning evolves in distinct ways across the model suite, highlighting the impact of internal architecture on system dynamics (Figure 7.7).

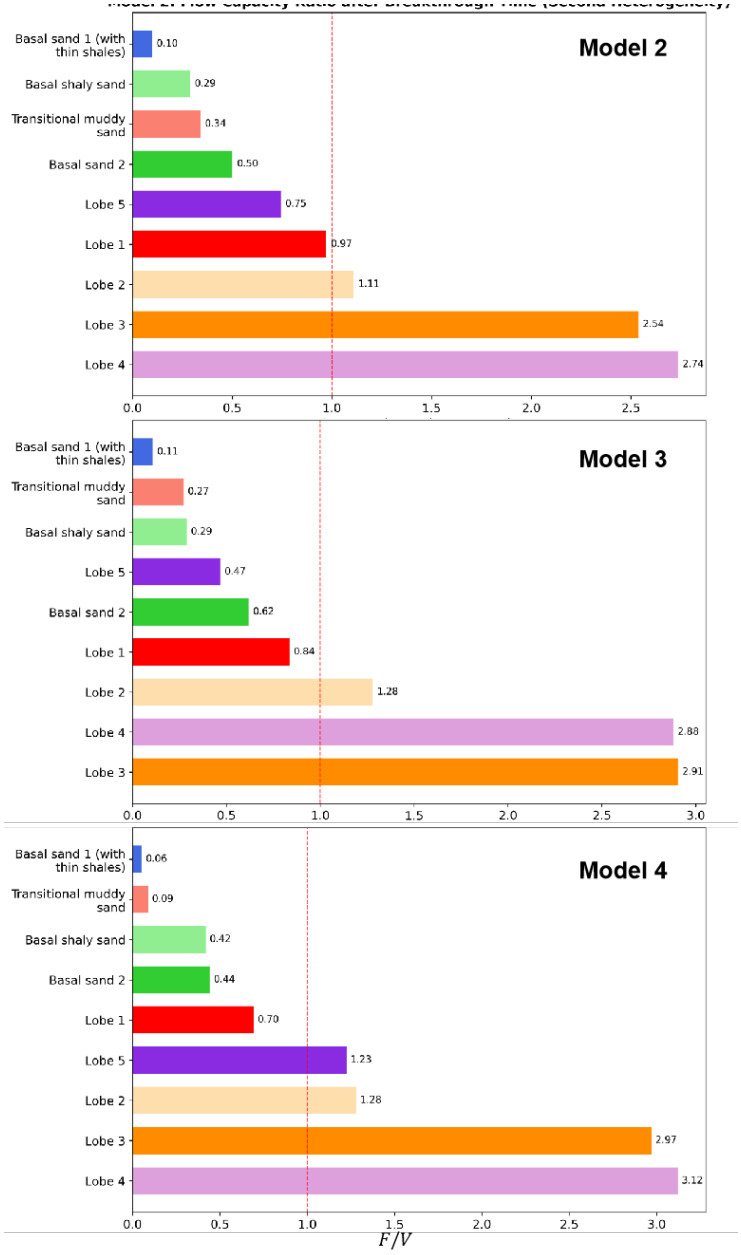

Figure 7.7: F/V Distribution at L2 Scale. Comparison across Model 2-4 at Model 2's Breakthrough Time (16.44 years).

In the simpler Model L2, a clear flow redistribution is observed. Lobe 2 becomes an active flow path ($F/V = 1.1$), and Lobe 1 approaches neutrality (0.97). Meanwhile, the dominance of the primary conduits, Lobe 3 (2.54) and Lobe 4 (2.74), decreases as they become more saturated. This pattern indicates a sequential filling behavior in simpler architectures: after the most efficient pathways are utilized, flow is diverted to previously underutilized units.

In Model L3, the flow structure exhibits greater stability. The F/V ratios of the key lobes (Lobe 3: 2.91; Lobe 4: 2.88) remain close to their 10-year values, suggesting that the internal sub-lobe network provides sustained and distributed flow capacity, preventing rapid saturation of the main pathways.

The response of Model L4 is the most revealing. The high-efficiency Lobe 3 (2.97) and Lobe 4 (3.12) continue to increase their flow share, while the contributions from secondary lobes (Lobe 2: 1.28; Lobe 5: 1.23) decrease. This demonstrates a flow localization effect in the most complex model: the finest-scale heterogeneities create efficient and entrenched conduits within the best lobes that capture an ever-increasing fraction of the injected fluid, thereby suppressing the activation of surrounding units.

7.3.3. 100 Years

By the 100-year mark, the flow partitioning undergoes a significant homogenization across all models, signaling a transition from early-stage channeling toward a more balanced sweep (Figure 7.8).

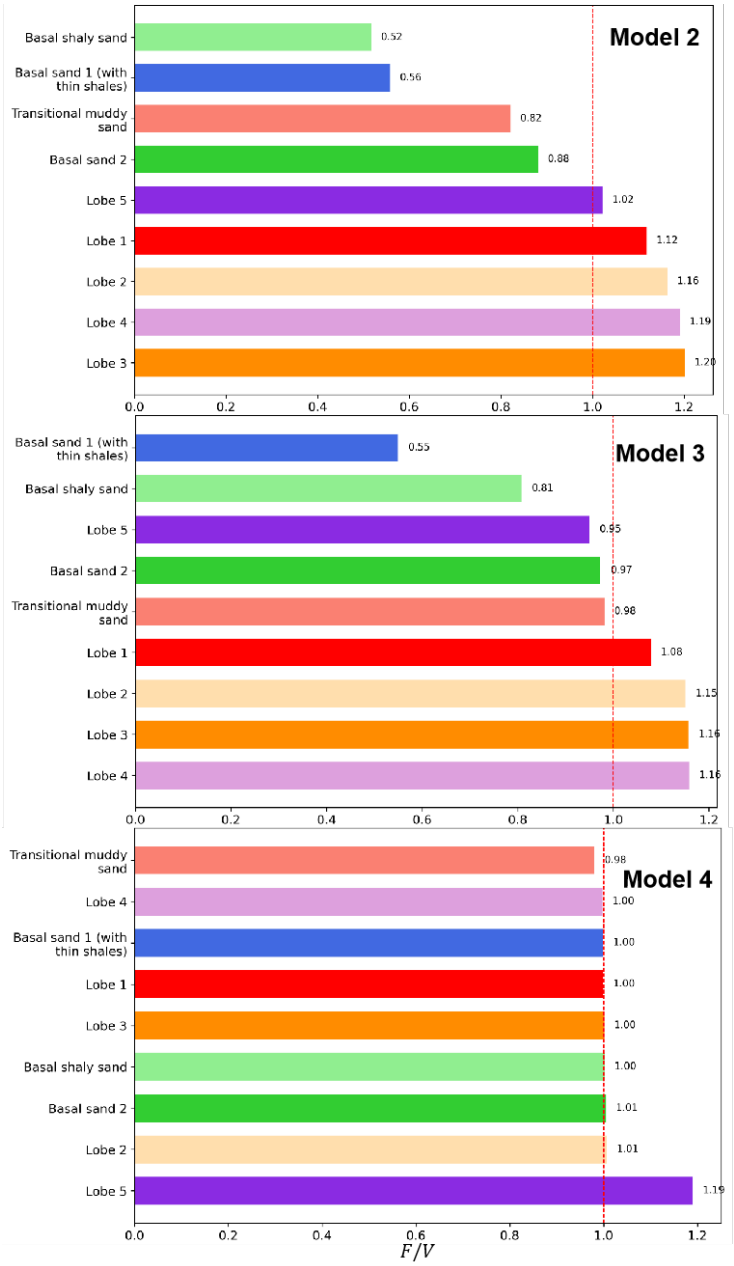

Figure 7.8: F/V Distribution at L2 Scale. Comparison across Model 2-4 at 100 years.

In Model L2, the extreme flow dominance observed earlier has diminished. All five upper lobes have now become active flow paths, with their F/V ratios converging into a narrow, near-neutral band between 1.02 and 1.29. This indicates a well-balanced, post-breakthrough equilibration where the injected fluid

finally achieves a relatively uniform sweep of the reservoir's primary storage volume.

In Model L3, this trend toward equilibrium is even more pronounced. The F/V ratios of the lobes are nearly identical, clustering tightly between 1.08 and 1.16. Notably, units that were previously bypassed, such as the Transitional Layer (0.98) and Basal Sand 2 (0.97), are now on the verge of neutral sweep.

The state of Model L4 at 100 years is the most definitive. Except for Lobe 5 (1.19), which still receives a slight surplus of flow, the F/V ratios of all other units have converged to approximately 1.0. This represents the culmination of the equilibration process, showing that even the most entrenched "super-highways" present at early times have dissipated their dominance.

7.3.4. 1000 Years

Extending the analysis to 1000 years reveals the final, equilibrated state of the system. As illustrated in Figure 7.9, the F/V ratios for all geological units across Models L2 to L4 have converged to, or are asymptotically approaching, a value of 1. This convergence signifies that the dynamic flow partitioning has effectively ceased; the injected fluid now occupies the entire pore volume in proportion to its storage capacity, irrespective of the initial permeability architecture.

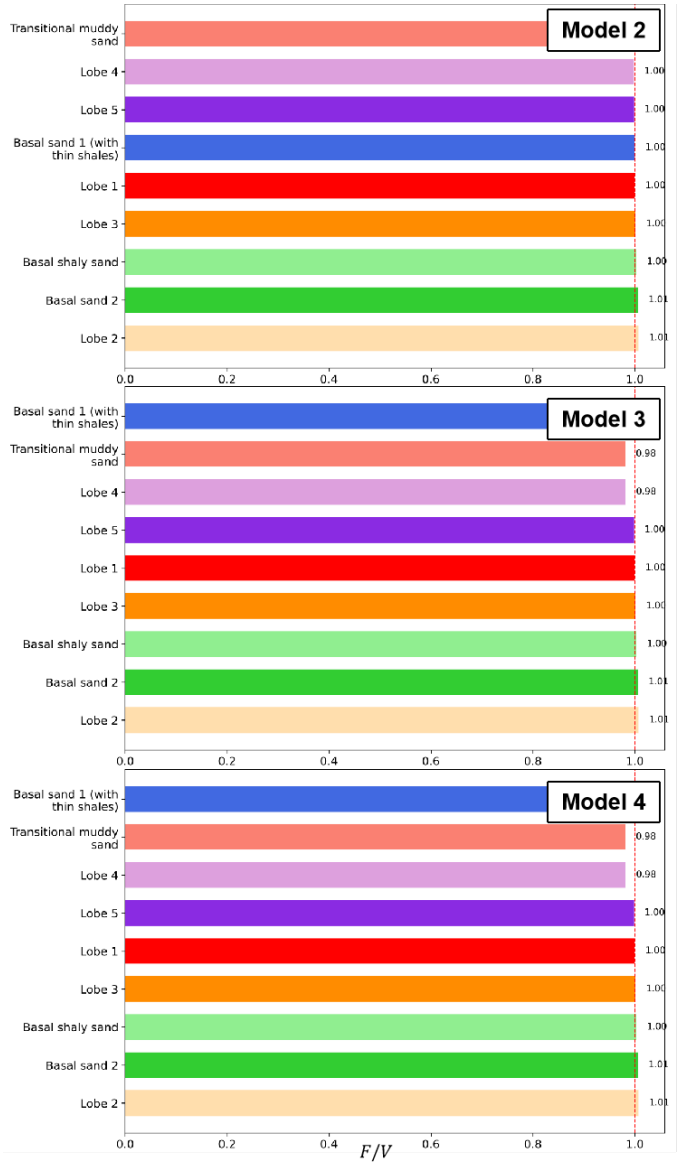

Figure 7.9: F/V Distribution at L2 Scale. Comparison across Model 2-4 at 1000 years.

8

Discussion

8.1. Flow Diagnostics Results Discussion

8.1.1. L1 Model: The Oversimplified Benchmark

The L1 Model primarily established the macroscopic flow boundary conditions, characterized by a simple, two-layer flow regime between the Upper and Lower Units (Figure 8.1). This oversimplified architecture fails to capture any internal fingering or small-scale heterogeneities, leading to a significant overestimation of reservoir performance. Consequently, the L1 Model yields the latest breakthrough time (22.26 years) and the highest recovery factor at 1 PVI (70.6%) among all scenarios (Figure 7.3).

The F/V analysis at the L1 scale further illustrates its limitations (Figure 7.5). At the 10-year, BT, and 100-year marks, the Upper Unit in Model L1 exhibits the lowest F/V ratio among all models, indicating a less concentrated flow distribution compared to its more complex counterparts. Furthermore, the minimal disparity in the F/V ratio between Upper and Lower Units directly reflects the model's inability to capture the high-permeability conduits that govern early-time flow in realistic systems.

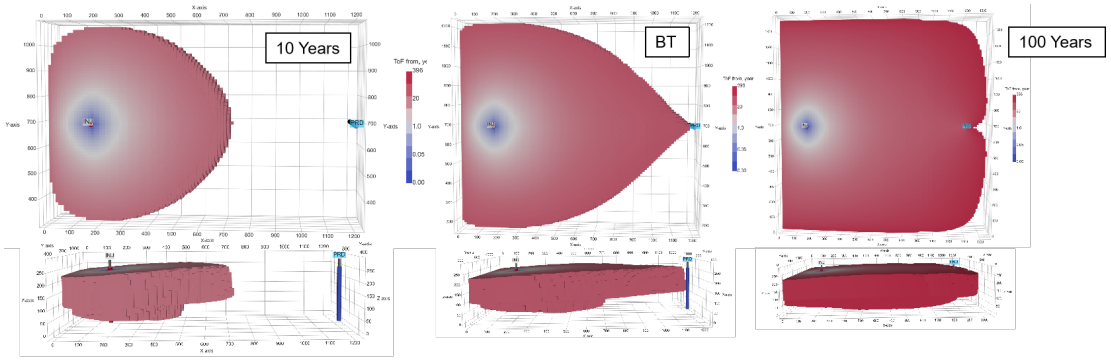

Figure 8.1: Flow diagnostics results (TOF) for model L1 in RRM, showing the CO_2 plume extent at 10 years, breakthrough time, and 100 years after injection start.

8.1.2. L2 Model: Revealing Dominant Pathways

The L2 Model demonstrates that the introduction of intermediate-scale architectural heterogeneity is the primary control on early-flow partitioning and the timing of breakthrough (Figure 8.2). The flow dynamics are not merely more complex than in L1; they are fundamentally governed by a different mechanism, the competition between a limited set of high-permeability conduits.

At the 10-year mark, a stable and distinct flow structure is already established. Lobes 3 and 4 emerge as dominant conduits, exhibiting significantly high F/V ratios of 3.69 and 3.25, respectively (Figure 7.6). This indicates that the injected fluid is predominantly channeled into and accumulates within these limited high-permeability units, resulting in highly focused flow.

This focused flow leads to a markedly earlier breakthrough time of 16.44 years compared to Model L1. At this critical moment, a redistribution of flow commences (Figure 7.7). While Lobes 3 and 4 remain

the primary pathways, their F/V values decrease as they become more saturated. Concurrently, the F/V ratios of the previously underutilized Lobes 2 and 1 rise to 1.10 and 0.97, respectively, signaling the sequential filling of the remaining heterogeneous units as the dominant pathways' capacity is reached.

By the 100-year mark, this sequential filling process continues and intensifies (Figure 7.8). The injected volume is progressively diverted into the secondary permeability units, leading to a significant homogenization of the F/V distribution. All five upper lobes converge into a narrow band of F/V ratios between 1.02 and 1.29, indicating a transition from early channeling to a more balanced, post-breakthrough sweep of the reservoir's primary storage volume.

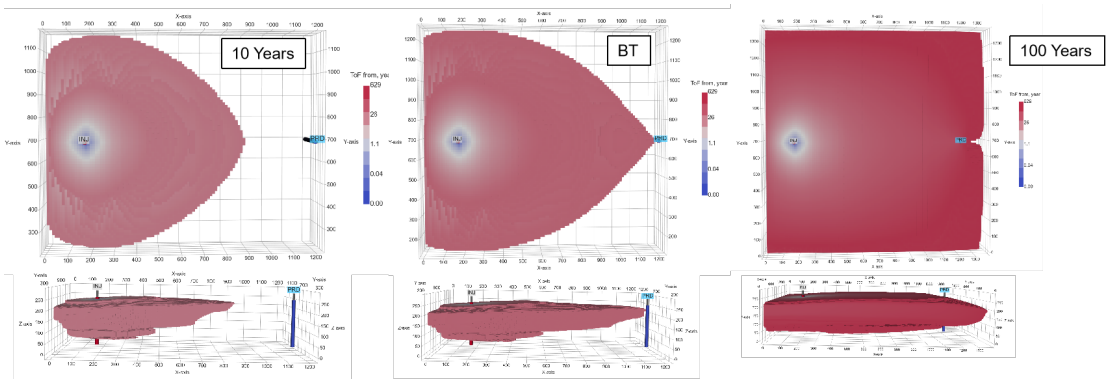

Figure 8.2: Flow diagnostics results (TOF) for model L2 in RRM, showing the CO_2 plume extent at 10 years, breakthrough time, and 100 years after injection start.

8.1.3. L4 Model: The Dual Narrative of Channeling and Equilibrium

The L4 Model demonstrates that fine-scale architectural heterogeneity introduces a dual control mechanism governing both early breakthrough and long-term equilibration (Figure 8.3).

At the 10-year mark, an intensified flow localization is already evident. Lobes 3 and 4 emerge as dominant conduits, exhibiting high F/V ratios of 2.74 and 2.91, respectively (Figure 7.6).

This intensified channeling leads to the earliest breakthrough time of 8.48 years among all models. At L2's breakthrough time (16.44 years), the flow polarization in L4 further intensifies (Figure 7.7). While Lobes 3 and 4 strengthen their dominance with F/V ratios rising to 2.97 and 3.12, respectively.

By the 100-year mark, however, a remarkable transition occurs (Figure 7.8). The F/V ratios for nearly all geological units converge to approximately 1.0, indicating that the dense network of small-scale heterogeneities enables efficient fluid redistribution across the entire system.

The behavior of L4 reveals that fine-scale heterogeneity creates a dual narrative. While it generates the most severe early-time channeling risk, it also possesses the inherent capacity for achieving a comprehensive long-term sweep.

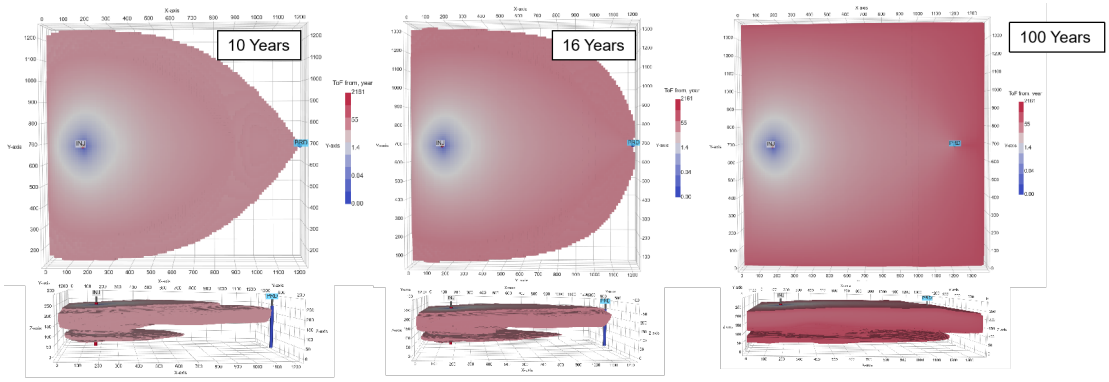

Figure 8.3: Flow diagnostics results (TOF) for model L4 in RRM, showing the CO_2 plume extent at 10 years, L2's breakthrough time, and 100 years after injection start.

8.1.4. L3 Model: The Balanced Compromise

The L3 Model demonstrates that sub-lobe scale heterogeneity establishes a balanced flow regime, exhibiting transitional behavior between the conduit-dominated flow of L2 and the polarized-equilibrated duality of L4 (Figure 8.4).

At the 10-year mark, a stable yet less dominant flow structure emerges. Lobes 3 and 4 function as primary conduits with F/V ratios of 3.01 and 3.03, respectively (Figure 7.6), values notably lower than their counterparts in the L2 Model. This indicates that while preferential pathways persist, their flow dominance is attenuated by the internal architectural subdivisions.

This moderated channeling leads to a breakthrough time of 10.81 years, positioned between L2 and L4. At L2's breakthrough time (16.44 years), the flow structure in L3 Model exhibits remarkable stability (Figure 7.7).

By the 100-year mark, the system shows advanced progression toward equilibrium (Figure 7.8). The F/V ratios of all lobes cluster tightly between 1.08 and 1.16, indicating a more uniform sweep than the L2 Model achieved at the same timeframe. This homogenization occurs without the extreme early polarization observed in the L4 Model, yet achieves comparable late-time efficiency.

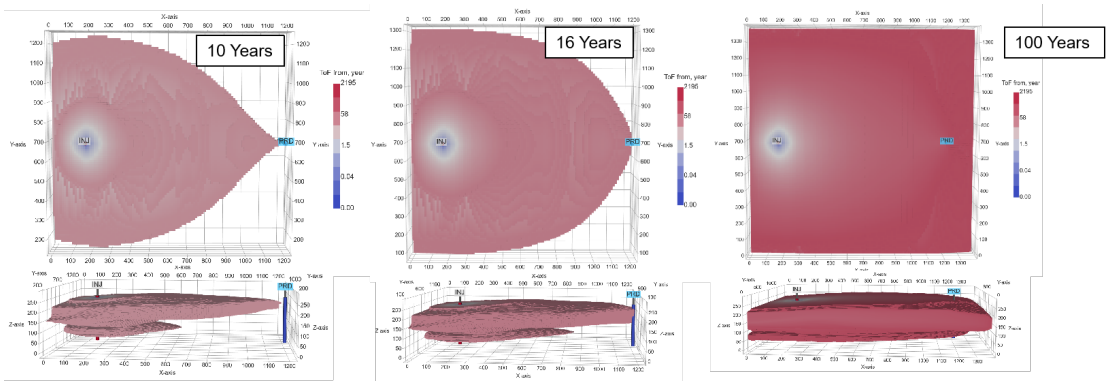

Figure 8.4: Flow diagnostics results (TOF) for model L3 in RRM, showing the CO_2 plume extent at 10 years, L2's breakthrough time, and 100 years after injection start.

8.1.5. Integrated Discussion and Conceptual Model

The systematic analysis from L1 to L4 reveals a non-linear relationship between geological complexity and CO_2 flow behavior. Rather than a simple progression, the models represent distinct archetypes, each governed by a unique flow mechanism with direct implications for storage performance and risk.

To synthesize these findings, a conceptual model is proposed (Figure 8.5), framing the archetypes along two key dimensions: 1) the intensity of early-flow dominance, and 2) the effort required for full system equilibration. This framework elucidates the fundamental trade-offs introduced by hierarchical heterogeneity.

Model L1, the homogeneous benchmark, occupies the domain of low dominance and low equilibration effort. Its simple structure lacks preferred pathways, allowing the fluid to approach a uniform distribution from the outset with minimal redistribution.

Model L2, in contrast, demonstrates that the introduction of intermediate-scale heterogeneity alone can create a system of high early dominance but also high equilibration effort. Its prominent conduits (Lobes 3, 4) capture the vast majority of early flow, but the lack of a finer-scale internal network results in a sluggish, step-wise sequential filling of secondary units (Lobes 2, 1), making the path to full equilibration inefficient.

Model L4 also represents the endpoint of high dominance and high equilibration effort. Its fine-scale heterogeneities create high-efficiency conduits that lead to rapid early breakthrough. However, the same complexities that facilitate channeling also create numerous, isolated low-flow regions. Achieving a balanced sweep of these regions requires overcoming significant flow barriers, making the path to full equilibration a challenging endeavor.

Model L3 once again emerges as a balanced compromise, situated between the extremes. It captures meaningful geological heterogeneity, resulting in a clearer flow hierarchy than L1, but avoids the extreme, effort-intensive polarization of L4.

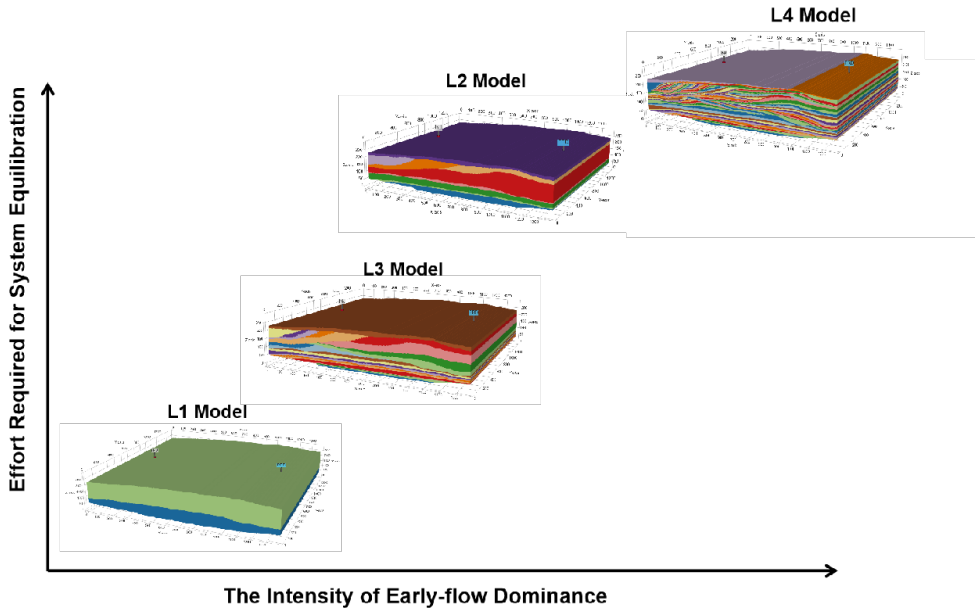

Figure 8.5: A Conceptual model relating early-flow dominance to the effort required for system equilibration, positioning the four model archetypes (L1-L4) within this framework.

8.2. Limitations and Future Work

8.2.1. Neglect of N-S Heterogeneity

A recognized limitation of the current hierarchical models is the simplified representation of heterogeneity along the N-S direction. Geological units were explicitly characterized and modeled only within E-W-oriented cross-sections. This approach implicitly assumes that all geological units extend homogeneously and with uniform thickness in the N-S direction, resulting in perfectly conformable contacts throughout the model (Figure 8.6).

This simplification does not fully capture the expected geological reality of a flood-tidal delta system. In particular, the lobate elements in the upper unit are likely to exhibit significant lateral variability in thickness and lobate geometry. The absence of this directional heterogeneity means that the current models may not accurately represent the full complexity of internal connectivity and potential flow baffling in the N-S direction, potentially leading to an overestimation of sweep efficiency perpendicular to the primary interpretation direction.

For future work, a key priority is to incorporate N-S heterogeneity to create more geologically realistic models. This could be achieved within the RRM software framework by utilizing the plan-view (map) window to delineate the lobate geometries of architectural elements directly. Integrating these map-view patterns with the existing E-W cross-sections would enable the construction of true 3D geological bodies that more faithfully reflect depositional architecture and significantly enhance the predictive capability of the models for flow simulations.

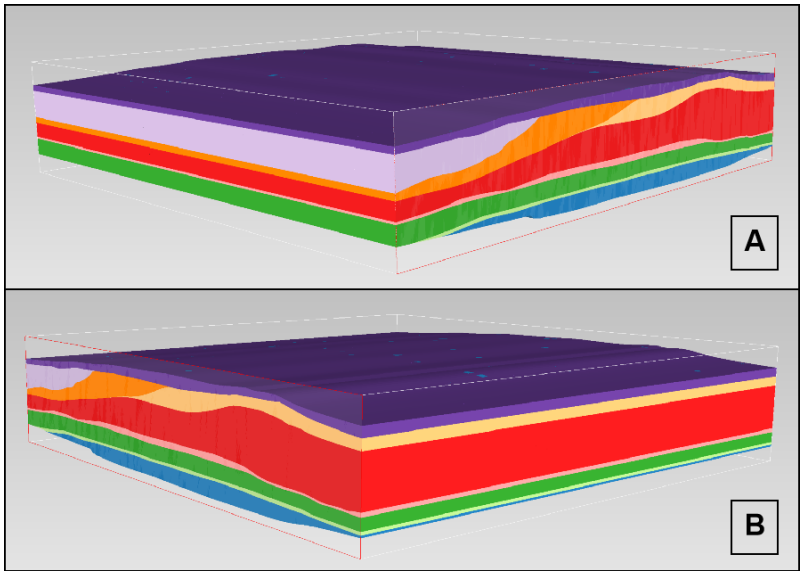

Figure 8.6: North-South view of Model L2 from (A) western and (B) eastern perspectives, illustrating the simplified representation with uniform unit thickness.

8.2.2. Limitations in Boundary Pressure

The flow diagnostics in this study employed a fixed production bottom-hole pressure of 1 bar to create a strong pressure sink and maximize the dynamic signal of heterogeneity. It is recognized that this value is not representative of a realistic field condition. In an actual CO_2 storage project, a production or pressure-management well would be maintained at a much higher pressure, typically close to the initial reservoir pressure.

A more physically realistic boundary condition would be to set the production pressure using a hydrostatic gradient. Future work should implement this refinement, calculating the initial reservoir pressure based on the model depth and assuming formation water density. Adopting such a boundary condition would enhance the field-scale relevance of the absolute quantitative predictions.

8.2.3. Considerations on Model Scaling

As noted in Chapter 6, the static models were constructed at a scale ten times larger than the original outcrop. This uniform scaling has a demonstrably negligible impact on the primary conclusions of this study for two key reasons.

First, the analysis relies predominantly on dimensionless parameters and ratios. Key metrics such as the volumetric proportion of geological units, the TOF proportion at a given time, and the ratio of TOF proportion and volumetric proportion are inherently dimensionless. These metrics are independent of the absolute physical dimensions of the system, as they describe proportional relationships and efficiencies rather than absolute quantities.

Second, and equally important, the same scaling factor was applied consistently to all models in the hierarchical series (L1–L4). In the context of a comparative study designed to isolate the effect of geological complexity, this scaling can be viewed as introducing a constant factor across all experimental cases. Since a constant multiplier does not alter the relative differences between the cases being compared, the observed trends and rankings in flow behavior across the L1–L4 models are preserved and remain robust.

Acknowledging the implications of this scaling is nevertheless important for the field applicability of the absolute results. The tenfold enlargement means that the pressure conditions and derived stress states in the simulation correspond to a reservoir at a significantly greater depth than the original outcrop. Future work should therefore focus on calibrating the flow simulations to pressure conditions representative of the actual outcrop's burial history to enhance the direct field-scale relevance of the absolute predictions.

8.2.4. Impact of Grid Resolution

The grid resolution analysis presented in Section 6.2 established a baseline for the simulations. However, a post-analysis of the simulation results, particularly from the L2–L4 models, revealed flow artifacts that suggest the selected resolution may have been insufficient to capture the connectivity within certain geological units fully.

Analysis of the TOF maps from the L2, L3, and L4 models showed an unexpected feature within Lobe 2: a distinct, roughly 20-meter-wide corridor where the CO_2 plume did not advance, creating a visible blank space in the TOF field (Figure 8.7). A related but distinct feature was observed in the TOF maps from the coarser (21^3 and 61^3) grids of the initial sensitivity study, which displayed a corridor of anomalously high TOF values in a similar location. In the benchmark models, this feature became less pronounced and ultimately vanished as the grid resolution was increased (Figure 8.8).

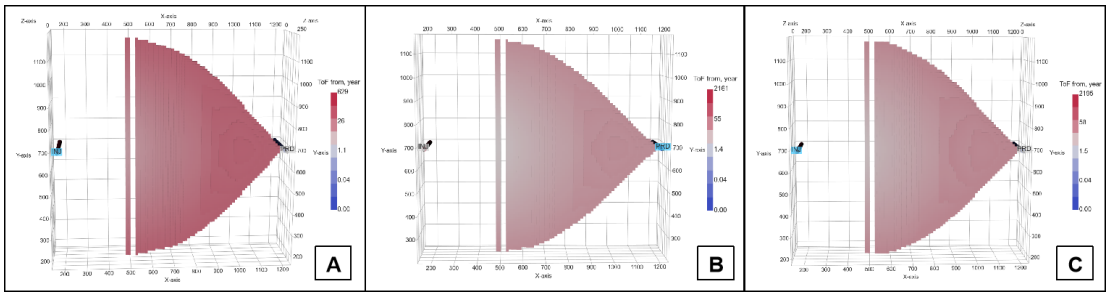

Figure 8.7: Breakthrough time TOF from maps for Lobe 2, comparing three distinct geological realizations: (A) L2 model, (B) L3 model, and (C) L4 model

The consistent occurrence of these features at lower resolutions, and their disappearance upon grid refinement strongly suggests they are a direct consequence of insufficient grid resolution. The grid was probably too coarse to accurately capture the full, continuous connectivity within the Lobe 2 unit. During the model population process, narrow, sinuous flow pathways at the boundaries of sedimentary bodies might not have been assigned the correct reservoir properties if their size was smaller than the grid cell dimensions. This would create discontinuous, blank, or effectively impermeable zones within an otherwise connected sand body. The solver then interprets these zones as barriers, forcing the CO_2 plume to bypass them and resulting in the observed blank or high-TOF corridors.

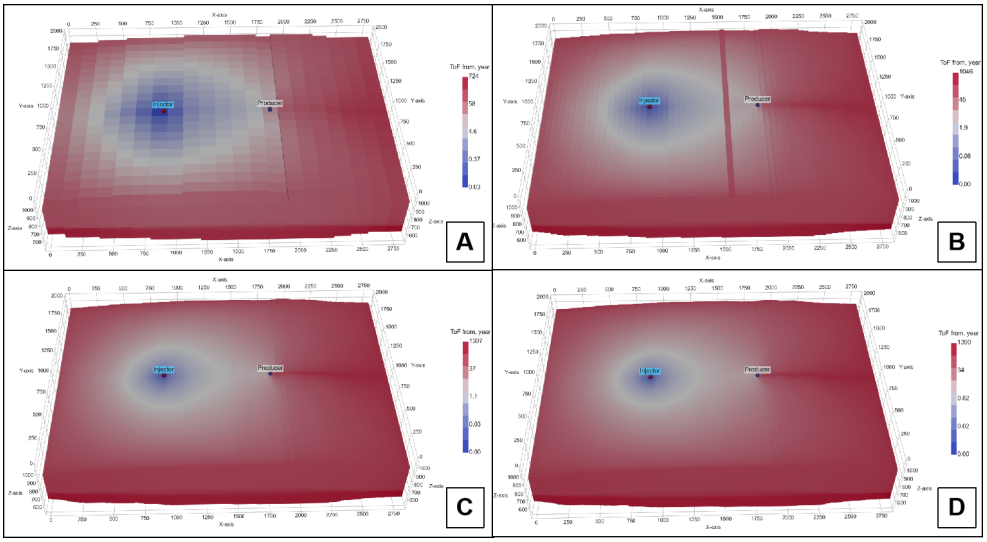

Figure 8.8: Ending time TOF from maps for benchmark model with varying grid resolutions: (A) 21×21×21, (B) 61×61×61, (C) 121×121×121, and (D) 161×161×161 grids.

Therefore, while global performance metrics had stabilized at the chosen resolution, the accurate

representation of local connectivity, particularly in geometrically complex units like Lobe 2, required a finer grid. The primary limitation identified is thus that the grid may not have fully resolved all small-scale flow pathways. Future work could employ higher-resolution grids to ensure that all geologically interpreted connectivity is correctly represented in the numerical model.

8.2.5. Limitations of Single-Phase Flow Diagnostics

The flow diagnostics methodology employed in this study provides a computationally efficient and powerful means to screen the impact of geological heterogeneity on connectivity and flow pathways. However, it is crucial to recognize that these simulations represent a single-phase tracer flow, which simplifies the complex multiphase physics of actual CO_2-brine displacement. Consequently, our results must be interpreted within the context of this key limitation.

In a real CO_2 storage scenario, three additional physical processes, which are not captured by our single-phase model, will fundamentally interact with and be influenced by geological heterogeneity:

1. **Buoyancy:** Due to the density contrast between CO_2 and brine, buoyancy is a dominant driving force for the upward migration of the CO_2 plume. Single-phase models cannot capture this vertical segregation and the resulting plume geometry.
2. **Capillary Forces:** Capillary forces are fundamental to both residual (snap-off) and capillary pinning trapping. The entry pressure of pore throats and heterogeneities, which dictates whether CO_2 is immobilized (pinned) or continues to migrate, is a quintessentially multiphase property. Single-phase flow diagnostics, by definition, have no concept of capillary entry pressure and thus completely overlook the critical mechanism of capillary pinning.
3. **Relative Permeabilities:** The simultaneous flow of CO_2 and brine is governed by their relative permeabilities, which describe how the presence of one phase impedes the flow of the other. This hysteresis and saturation-dependent behavior control the efficiency of displacement and the formation of residual CO_2 snap-off trapping.

The critical implication is that geological heterogeneities, which are the very drivers of capillary pinning, matter even more for trapping predictions than what single-phase diagnostics can reveal. A single-phase model might identify a high-permeability pathway, suggesting rapid CO_2 flow. However, a multiphase simulation could show that the same path is lined with small-scale, low-permeability laminae with high capillary entry pressures. These laminae would act as capillary barriers, pinning the CO_2 and diverting the plume laterally, leading to a trapping scenario vastly different from the single-phase prediction. Consequently, models that rely solely on single-phase diagnostics are likely to overestimate the migration velocity and lateral extent of the CO_2 plume while severely underestimating the total trapped volume, as they miss the significant contribution from capillary pinning.

9

Conclusion

This study was guided by two research questions, for which our hierarchical modeling workflow provides definitive answers:

Research Question 1

How can medium-scale discrete rock heterogeneities in flood-tidal delta deposits be effectively represented in static geological models for CO_2 storage applications?

The findings of this study clarify the essence of ”effective representation”: it is not the pursuit of maximum detail (L4), but the precise identification and incorporation of the geological features that dominantly control the target process (L2 and L3). The flow simulation results demonstrate that for CO_2 storage in flood-tidal delta systems, simply capturing the major lobes (L2) is necessary but insufficient for predicting reliable long-term dynamics. For predicting overall storage performance and equilibrium, representing the internal architecture of lobes (the L3 level) is the critical and most effective level of all models.

Research Question 2

How do medium-scale rock heterogeneities in flood-tidal delta deposits influence the CO_2 storage evolution as model complexity increases at short (1 to 100 years) time scales?

This study reveals a non-linear impact of geological complexity. The transition from the simplified two-layer L1 model to the more heterogeneous L2 model caused the most dramatic shift, reducing the CO_2 breakthrough time by over 40% and establishing a clear hierarchy of dominant flow conduits. This demonstrates that medium-scale architecture is the primary control on early plume migration and containment risk. Further increasing complexity to the L3 model moderated this channeling, yielding a more stable flow distribution and superior predictions of long-term sweep efficiency. In contrast, the most complex L4 model exhibited a dual narrative: it intensified early flow polarization, leading to the earliest breakthrough, yet its dense heterogeneity network also facilitated the most rapid system-wide equilibration over centuries.

The key conclusion is that while all heterogeneous models accelerate CO_2 migration, the relationship is not monotonic. For forecasting, the L2 model is sufficient to identify the primary leakage risks, but the L3 model provides the most robust and balanced prediction of overall storage performance, effectively capturing the critical heterogeneity without the predictive extremes of the most complex realizations.

References

[1] David I Armstrong McKay et al. “Exceeding 1.5 °C global warming could trigger multiple climate tipping points”. In: *Science* 377.6611 (2022), eabn7950.

[2] Samuel Krevor et al. “Subsurface carbon dioxide and hydrogen storage for a sustainable energy future”. In: *Nature Reviews Earth & Environment* 4.2 (2023), pp. 102–118.

[3] Stefan Bachu. “CO2 storage in geological media: Role, means, status and barriers to deployment”. In: *Progress in energy and combustion science* 34.2 (2008), pp. 254–273.

[4] Peter Kelemen et al. “An overview of the status and challenges of CO2 storage in minerals and geological formations”. In: *Frontiers in Climate* 1 (2019), p. 9.

[5] Mai Bui et al. “Carbon capture and storage (CCS): the way forward”. In: *Energy & Environmental Science* 11.5 (2018), pp. 1062–1176.

[6] Silvia De Simone et al. “A tool for first order estimates and optimisation of dynamic storage resource capacity in saline aquifers”. In: *International Journal of Greenhouse Gas Control* 106 (2021), p. 103258.

[7] Samuel Krevor et al. “Capillary trapping for geologic carbon dioxide storage–From pore scale physics to field scale implications”. In: *International Journal of Greenhouse Gas Control* 40 (2015), pp. 221–237.

[8] Edward Rubin et al. “IPCC special report on carbon dioxide capture and storage”. In: *UK: Cambridge University Press. TNO (2004): Cost Curves for CO2 Storage, Part* 2 (2005), p. 14.

[9] Qin Zhang et al. “Capillary pinning in sedimentary rocks for CO2 storage: Mechanisms, terminology and State-of-the-Art”. In: *International Journal of Greenhouse Gas Control* 144 (2025), p. 104385. DOI: https://doi.org/10.1016/j.ijggc.2025.104385. URL: https://www.sciencedirect.com/science/article/pii/S1750583625000830.

[10] Matthew Andrew et al. “Pore-scale contact angle measurements at reservoir conditions using X-ray microtomography”. In: *Advances in Water resources* 68 (2014), pp. 24–31.

[11] Ehsan Saadatpoor et al. “New trapping mechanism in carbon sequestration”. In: *Transport in porous media* 82.1 (2010), pp. 3–17.

[12] Naum I Gershenzon et al. “Capillary trapping of CO2 in heterogeneous reservoirs during the injection period”. In: *International Journal of greenhouse gas control* 59 (2017), pp. 13–23.

[13] Mark Bentley et al. “Storage v. production: challenges for reservoir modelling and simulation practitioners”. In: *Geological Society, London, Energy Geoscience Conference Series*. Vol. 1. 1. The Geological Society of London. 2026, egc1–2024.

[14] Christopher W MacMinn et al. “CO2 migration in saline aquifers. Part 1. Capillary trapping under slope and groundwater flow”. In: *Journal of fluid mechanics* 662 (2010), pp. 329–351.

[15] Madeleine J Golding et al. “Two-phase gravity currents in porous media”. In: *Journal of fluid mechanics* 678 (2011), pp. 248–270.

[16] Marinus Eric Donselaar. *Barrier island coasts and relative sea level rise: preservation potential, facies architecture and sequence analysis*. PhD thesis, Delft University of Technology, 1996.

[17] Jaume Vergés et al. “South Pyrenean fold and thrust belt: The role of foreland evaporitic levels in thrust geometry”. In: *Thrust tectonics*. Springer, 1992, pp. 255–264.

[18] Pablo Santolaria et al. “Formation and growth of diapirs in contractional settings: the Mediano anticline and Clamosa diapir case study (Southern Pyrenees)”. In: *Solid Earth* 16.10 (2025), pp. 899–927.

[19] Josep Anton Muñoz et al. “The structure of the South-Central-Pyrenean fold and thrust belt as constrained by subsurface data”. In: *Geologica Acta: an international earth science journal* 16.4 (2018), pp. 439–460.

[20] Josep Poblet et al. “Quantifying the kinematics of detachment folds using three-dimensional geometry: Application to the Mediano anticline (Pyrenees, Spain)”. In: *Geological Society of America Bulletin* 110.1 (1998), pp. 111–125.

[21] Tania Mochales et al. “Rotational velocity for oblique structures (Boltaña anticline, Southern Pyrenees)”. In: *Journal of Structural Geology* 35 (2012), pp. 2–16.

[22] Swie-Djin Nio et al. *Field Guide to Transgressive Silici-clastic Complexes in the Southern Pyrenean Basin, Spain*. Sedimentology Group, State University of Utrecht, 1978.

[23] Margarita Cuevas Gozalo. “Geometry and lithofacies of sediment bodies in a tidally influenced alluvial area. Middle Eocene, Southern Pyrenees, Spain”. In: *Netherlands Journal of Geosciences* (1985), pp. 221–231.

[24] James Iain Scotchman. “Stratigraphic context and timing of sand supply to deep-marine Ainsa-Jaca basin, middle Eocene, Spanish Pyrenees: Constraints from geochemistry and sedimentology”. PhD thesis. UCL (University College London), 2012.

[25] JI Scotchman et al. “A new age model for the middle Eocene deep-marine Ainsa Basin, Spanish Pyrenees”. In: *Earth-Science Reviews* 144 (2015), pp. 10–22.

[26] RP Speijer et al. “The paleogene period”. In: *Geologic time scale 2020*. Elsevier, 2020, pp. 1087–1140.

[27] Rick Donselaar et al. “An Eocene tidal inlet/washover type barrier island complex in the south Pyrenean marginal basin”. In: *Geologie en Mijnbouw/Netherlands Journal of Geosciences* 61 (1982), pp. 343–353.

[28] Miles O Hayes. “General morphology and sediment patterns in tidal inlets”. In: *Sedimentary geology* 26.1-3 (1980), pp. 139–156.

[29] SD Nio et al. “Sea-level fluctuations and the geometric variability of tide-dominated sandbodies”. In: *Sedimentary Geology* 70.2-4 (1991), pp. 161–193.

[30] Kathrine Torgersen. “Modeling the effects of detailed geological architecture on CO2 storage using the Pano Lagoonal barrier-bar system outcrop (Spain)”. MA thesis. NTNU, 2024.

[31] AW Martinius et al. *Atlas of sedimentary structures in estuarine and tidally-influenced river deposits of the Rhine-Meuse-Scheldt system*. EAGE Houten, 2011.

[32] MO Hayes. “Barrier island morphology as a function of tidal and wave regime. In: Leatherman SP (ed) Barrier Islands”. In: *Academic Press, New York* 1 (1979), p. 27.

[33] Duncan M FitzGerald. “Geomorphic variability and morphologic and sedimentologic controls on tidal inlets”. In: *Journal of Coastal Research* (1996), pp. 47–71.

[34] Duncan FitzGerald et al. “Morphodynamics and Facies Architecture of Tidal Inlets and Tidal Deltas”. In: *Principles of Tidal Sedimentology*. Ed. by Richard A. Davis Jr. et al. Dordrecht: Springer Netherlands, 2012, pp. 301–333. DOI: 10.1007/978-94-007-0123-6_12. URL: https://doi.org/10.1007/978-94-007-0123-6_12.

[35] M. Royhan Gani. “Chapter 14 - Clastic shorelines and deltas”. In: *Regional Geology and Tectonics (Second Edition)*. Ed. by Nicola Scarselli et al. Second Edition. Elsevier, 2020, pp. 343–364. DOI: https://doi.org/10.1016/B978-0-444-64134-2.00012-2. URL: https://www.sciencedirect.com/science/article/pii/B9780444641342000122.

[36] M Royhan Gani et al. “Lithostratigraphy versus chronostratigraphy in facies correlations of Quaternary deltas: Application of bedding correlation”. In: (2005).

[37] Enrica Mutti et al. “Delta-front facies associations of ancient flood-dominated fluvio-deltaic systems”. In: *Revista de la Sociedad Geológica de España* 13.2 (2000), pp. 165–190.

[38] Shedid A. Shedid. “Vertical-horizontal permeability correlations using coring data”. In: *Egyptian Journal of Petroleum* 28.1 (2019), pp. 97–101. DOI: https://doi.org/10.1016/j.ejpe.2018.12.007. URL: https://www.sciencedirect.com/science/article/pii/S1110062118301429.

[39] Carl Jacquemyn et al. “Sketch-based interface and modelling of stratigraphy and structure in three dimensions”. In: *Journal of the Geological Society* 178.4 (2021), jgs2020–187.

[40] Dmytro Petrovskyy et al. “Rapid flow diagnostics for prototyping of reservoir concepts and models for subsurface CO2 storage”. In: *International Journal of Greenhouse Gas Control* 124 (2023), p. 103855.

[41] Guillaume Caumon et al. “Surface-based 3D modeling of geological structures”. In: *Mathematical geosciences* 41.8 (2009), pp. 927–945.

[42] William A Jackson et al. “A screening assessment of the impact of sedimentological heterogeneity on CO2 migration and stratigraphic-baffling potential: Johansen and Cook formations, Northern Lights project, offshore Norway”. In: *International Journal of Greenhouse Gas Control* 120 (2022), p. 103762.

[43] Jafar Alshakri et al. “A screening assessment of the impact of sedimentological heterogeneity on CO2 migration and stratigraphic-baffling potential: Sherwood and Bunter sandstones, UK”. In: (2023).

[44] Zhao Zhang et al. “Fast flow computation methods on unstructured tetrahedral meshes for rapid reservoir modelling”. In: *ECMOR XVI-16th European Conference on the Mathematics of Oil Recovery*. Vol. 2018. 1. European Association of Geoscientists & Engineers. 2018, pp. 1–15.

[45] Olav Møyner et al. “The application of flow diagnostics for reservoir management”. In: *SPE Journal* 20.02 (2015), pp. 306–323.

[46] Mohammad Shahvali et al. “An alternative to streamlines for flow diagnostics on structured and unstructured grids”. In: *SPE Journal* 17.03 (2012), pp. 768–778.

[47] JP Schmalz et al. “The variation of waterflood performance with variation in permeability profile”. In: *Prod. Monthly* 15.9 (1950), pp. 9–12.

[48] Peter B. Flemings. “Overburden Stress, Least Principal Stress, and Fracture Initiation Pressure”. In: *A Concise Guide to Geopressure: Origin, Prediction, and Applications*. Cambridge University Press, 2021, pp. 167–193.

A

Appendix

A.1. Geological Background

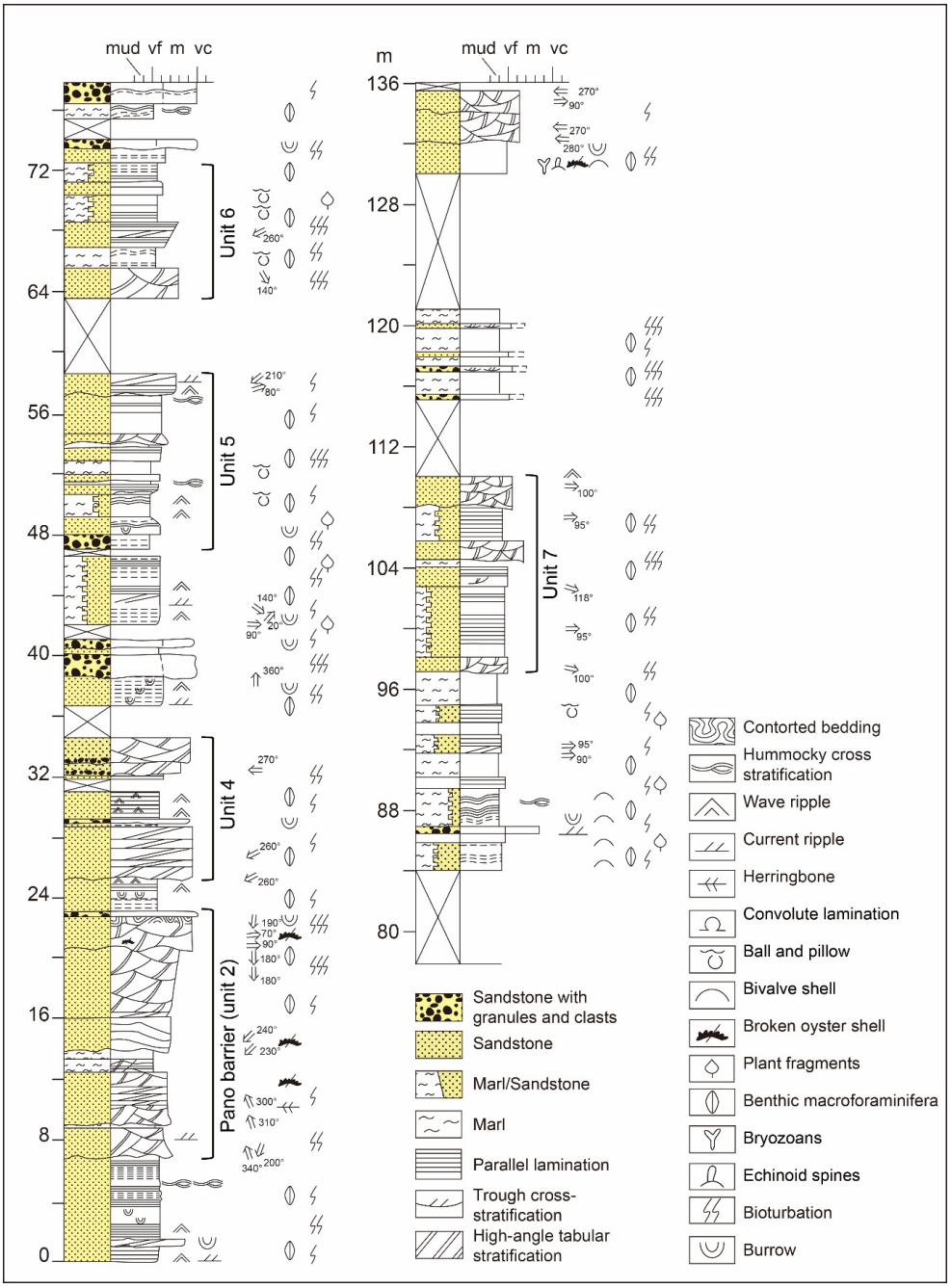

Figure A.1: Measured succession exposed at the village of Pano measured along an inclined trajectory showing 5 main sandstone intervals. This succession is interpreted as formed in an open marine shallow-water embayment. Successive sandstone intervals are possibly related to some of the stratigraphically younger and more south-eastward located flood-tidal delta deposits such as those near the villages of Pocino and Panillo and provisionally interpreted as ebb-tidal delta deposits vertically stacked in a retrogradational fashion. Modified after Hulten and Bootsman (1975).

A.2. Datasets and Input Data

Table A.1: Detailed petrophysical property assignment for the L1 (Lowest Complexity) model.

Model ID	Layer ID	Facies Type	Relative Quality	ϕ (%)	k_{xy} (mD)	k_z (mD)	k_v/k_h
L1	U1	Shaly Sand	Low–medium	13.5	50	10	0.2
L1	U2	Clean Sand	Medium–good	17.5	150	30	0.2

Table A.2: Detailed petrophysical property assignment for the L2 (Intermediate Complexity) model.

Model ID	Layer ID	Facies Type	Relative Quality	ϕ (%)	k_{xy} (mD)	k_z (mD)	k_v/k_h
L2	U1	Shaly Sand	Low–medium	13.5	30	6	0.2
L2	U2	Mudstone	Very low	7.5	1	0.2	0.2
L2	U3	Shaly Sand	Medium	13.5	50	10	0.2
L2	U4	Mudstone	Low	7.5	1	0.2	0.2
L2	U5	Shaly Sand+Clean Sand	High	15.5	120	24	0.2
L2	U6	Shaly Sand+Clean Sand	Medium–good	15.5	150	30	0.2
L2	U7	Clean Sand	High	17.5	200	40	0.2
L2	U8	Clean Sand	High	17.5	300	60	0.2
L2	U9	Shaly Sand	Medium–good	13.5	60	12	0.2

Table A.3: Detailed petrophysical property assignment for the L3 (High Complexity) model.

Model ID	Layer ID	Facies Type	Relative Quality	ϕ (%)	k_{xy} (mD)	k_z (mD)	k_v/k_h
L3	U1	Shaly Sand	Low–medium	13.5	20	4	0.2
L3	U2	Mudstone	Very low	7.5	1	0.2	0.2
L3	U3	Shaly Sand	Low–medium	13.5	30	6	0.2
L3	U4	Mudstone	Very low	7.5	1	0.2	0.2
L3	U5	Shaly Sand	Low–medium	13.5	40	8	0.2
L3	U6	Shaly Sand	Low–medium	13.5	50	10	0.2
L3	U7	Shaly Sand	Low	13.5	20	4	0.2
L3	U8	Clean Sand	Medium	17.5	100	20	0.2
L3	U9	Clean Sand	Medium	17.5	120	24	0.2
L3	U10	Clean Sand	Medium	17.5	110	22	0.2
L3	U11	Shaly Sand	Low–medium	13.5	30	6	0.2
L3	U12	Shaly Sand	Medium	13.5	50	10	0.2
L3	U13	Clean Sand	Medium–good	17.5	150	30	0.2
L3	U14	Shaly Sand	Medium	13.5	60	12	0.2
L3	U15	Shaly Sand + Clean Sand	Medium–good	15.5	150	30	0.2
L3	U16	Shaly Sand + Clean Sand	High	15.5	200	40	0.2

Continued on next page

Table A.3 – Continued from previous page

Model ID	Layer ID	Facies Type	Relative Quality	ϕ (%)	k_{xy} (mD)	k_z (mD)	k_v/k_h
L3	U17	Shaly Sand + Clean Sand	High	15.5	220	44	0.2
L3	U18	Clean Sand	High	17.5	300	60	0.2
L3	U19	Clean Sand	High	17.5	400	80	0.2
L3	U20	Clean Sand	High	17.5	500	100	0.2
L3	U21	Clean Sand	High	17.5	400	80	0.2
L3	U22	Clean Sand	High	17.5	300	60	0.2
L3	U23	Shaly Sand	Medium–good	13.5	50	10	0.2

Table A.4: Detailed petrophysical property assignment for the L4 (Highest Complexity) model.

Model ID	Layer ID	Facies Type	Relative Quality	ϕ (%)	k_{xy} (mD)	k_z (mD)	k_v/k_h
L4	U1	Shaly Sand	Low–medium	13.5	20	4	0.2
L4	U2	Mudstone	Very low	7.5	1	0.2	0.2
L4	U3	Shaly Sand	Low–medium	13.5	30	6	0.2
L4	U4	Mudstone	Very low	7.5	1	0.2	0.2
L4	U5	Shaly Sand + Mudstone	Low	10.5	10	2	0.2
L4	U6	Shaly Sand + Mudstone	Low	10.5	8	1.6	0.2
L4	U7	Shaly Sand	Low	13.5	20	4	0.2
L4	U8	Shaly Sand + Clean Sand	Low–medium	15.5	100	20	0.2
L4	U9	Shaly Sand + Mudstone	Low	10.5	10	2	0.2
L4	U10	Shaly Sand + Clean Sand	Medium	15.5	120	24	0.2
L4	U11	Shaly Sand + Clean Sand	Medium	15.5	120	24	0.2
L4	U12	Shaly Sand	Low–medium	13.5	30	6	0.2
L4	U13	Shaly Sand + Mudstone	Low	10.5	10	2	0.2
L4	U14	Shaly Sand	Low–medium	13.5	30	6	0.2
L4	U15	Shaly Sand + Mudstone	Low	10.5	10	2	0.2
L4	U16	Shaly Sand	Low–medium	13.5	30	6	0.2
L4	U17	Shaly Sand	Low–medium	13.5	30	6	0.2
L4	U18	Clean Sand	Medium	17.5	120	24	0.2
L4	U19	Clean Sand	Medium	17.5	140	28	0.2
L4	U20	Clean Sand	Medium–good	17.5	150	30	0.2
L4	U21	Clean Sand	Medium–good	17.5	160	32	0.2
L4	U22	Clean Sand	Medium–good	17.5	170	34	0.2
L4	U23	Clean Sand	Medium–good	17.5	180	36	0.2
L4	U24	Shaly Sand + Mudstone	Low–medium	10.5	10	2	0.2

Continued on next page

Table A.4 – Continued from previous page

Model ID	Layer ID	Facies Type	Relative Quality	ϕ (%)	k_{xy} (mD)	k_z (mD)	k_v/k_h
L4	U25	Shaly Sand + Mudstone	Low–medium	10.5	10	2	0.2
L4	U26	Shaly Sand + Mudstone	Low–medium	10.5	10	2	0.2
L4	U27	Shaly Sand	Medium	13.5	60	12	0.2
L4	U28	Shaly Sand + Clean Sand	Medium	15.5	130	26	0.2
L4	U29	Shaly Sand + Clean Sand	Medium	15.5	140	28	0.2
L4	U30	Shaly Sand + Clean Sand	Medium	15.5	150	30	0.2
L4	U31	Shaly Sand + Clean Sand	Medium–good	15.5	160	32	0.2
L4	U32	Shaly Sand + Clean Sand	Medium–good	15.5	170	34	0.2
L4	U33	Shaly Sand + Clean Sand	Medium–good	15.5	180	36	0.2
L4	U34	Shaly Sand + Clean Sand	Medium–good	15.5	190	38	0.2
L4	U35	Shaly Sand + Clean Sand	Medium–good	15.5	200	40	0.2
L4	U36	Shaly Sand + Clean Sand	Medium–good	15.5	210	42	0.2
L4	U37	Shaly Sand + Clean Sand	Medium–good	15.5	220	44	0.2
L4	U38	Shaly Sand + Clean Sand	Medium–good	15.5	230	46	0.2
L4	U39	Shaly Sand + Clean Sand	Good-high	15.5	250	50	0.2
L4	U40	Shaly Sand + Clean Sand	Good-high	15.5	260	52	0.2
L4	U41	Clean Sand	Good-high	17.5	270	54	0.2
L4	U42	Clean Sand	Good-high	17.5	280	56	0.2
L4	U43	Clean Sand	Good-high	17.5	290	58	0.2
L4	U44	Clean Sand	Good-high	17.5	300	60	0.2
L4	U45	Clean Sand	Good-high	17.5	310	62	0.2
L4	U46	Clean Sand	Good-high	17.5	320	64	0.2
L4	U47	Clean Sand	Good-high	17.5	330	66	0.2
L4	U48	Clean Sand	Good-high	17.5	340	68	0.2
L4	U49	Clean Sand	Good-high	17.5	350	70	0.2
L4	U50	Clean Sand	Good-high	17.5	360	72	0.2
L4	U51	Clean Sand	Good-high	17.5	370	74	0.2
L4	U52	Clean Sand	Good-high	17.5	380	76	0.2
L4	U53	Clean Sand	Good-high	17.5	390	78	0.2
L4	U54	Clean Sand	Good-high	17.5	310	62	0.2
L4	U55	Clean Sand	Good-high	17.5	320	64	0.2
L4	U56	Clean Sand	Good-high	17.5	330	66	0.2
L4	U57	Clean Sand	Good-high	17.5	340	68	0.2
L4	U58	Clean Sand	Good-high	17.5	350	70	0.2

Continued on next page

Table A.4 – Continued from previous page

Model ID	Layer ID	Facies Type	Relative Quality	ϕ (%)	k_{xy} (mD)	k_z (mD)	k_v/k_h
L4	U59	Clean Sand	Good-high	17.5	360	72	0.2
L4	U60	Clean Sand	Good-high	17.5	370	74	0.2
L4	U61	Clean Sand	Good-high	17.5	380	76	0.2
L4	U62	Clean Sand	Good-high	17.5	390	78	0.2
L4	U63	Clean Sand	Good-high	17.5	400	80	0.2
L4	U64	Clean Sand	Good-high	17.5	410	82	0.2
L4	U65	Clean Sand	Good-high	17.5	420	84	0.2
L4	U66	Clean Sand	Good-high	17.5	430	86	0.2
L4	U67	Clean Sand	Good-high	17.5	440	88	0.2
L4	U68	Clean Sand	Good-high	17.5	450	90	0.2
L4	U69	Clean Sand	Good-high	17.5	460	92	0.2
L4	U70	Clean Sand	Good-high	17.5	470	94	0.2
L4	U71	Clean Sand	Good-high	17.5	480	96	0.2
L4	U72	Clean Sand	Good-high	17.5	310	62	0.2
L4	U73	Clean Sand	Good-high	17.5	320	64	0.2
L4	U74	Clean Sand	Good-high	17.5	330	66	0.2
L4	U75	Clean Sand	Good-high	17.5	340	68	0.2
L4	U76	Clean Sand	Good-high	17.5	350	70	0.2
L4	U77	Clean Sand	Good-high	17.5	360	72	0.2
L4	U78	Clean Sand	High	17.5	450	90	0.2
L4	U79	Clean Sand	High	17.5	460	92	0.2
L4	U80	Clean Sand	High	17.5	470	94	0.2
L4	U81	Clean Sand	High	17.5	480	96	0.2
L4	U82	Clean Sand	High	17.5	490	98	0.2
L4	U83	Clean Sand	High	17.5	500	100	0.2
L4	U84	Clean Sand	High	17.5	510	102	0.2
L4	U85	Clean Sand	High	17.5	520	104	0.2
L4	U86	Clean Sand	High	17.5	530	106	0.2
L4	U87	Clean Sand	Good-high	17.5	310	62	0.2
L4	U88	Clean Sand	Good-high	17.5	320	64	0.2
L4	U89	Clean Sand	Good-high	17.5	330	66	0.2
L4	U90	Clean Sand	Good-high	17.5	340	68	0.2
L4	U91	Clean Sand	Good-high	17.5	350	70	0.2
L4	U92	Clean Sand	Good-high	17.5	360	72	0.2
L4	U93	Clean Sand	Good-high	17.5	370	74	0.2
L4	U94	Clean Sand	Good-high	17.5	380	76	0.2
L4	U95	Shaly Sand + Clean Sand	Medium–good	15.5	150	30	0.2
L4	U96	Shaly Sand + Clean Sand	Medium–good	15.5	160	32	0.2
L4	U97	Shaly Sand + Clean Sand	Medium–good	15.5	170	34	0.2
L4	U98	Shaly Sand + Clean Sand	Medium–good	15.5	180	36	0.2
L4	U99	Shaly Sand + Clean Sand	Medium–good	15.5	190	38	0.2
L4	U100	Shaly Sand + Clean Sand	Medium–good	15.5	200	40	0.2

A.3. Flow Diagnostics

Table A.5: Summary of key parameters and simulation results for Model L1.

Parameter	Value / Description
Model Name	L1 model
Grid Dimensions	121,121,121
Number of Layers (Z)	2
Injection Rate	3541 m³/day
Flow Rate	22.27 Mbbl/day
Breakthrough Time (INJ)	22.26 years
Breakthrough Time (PRD)	22.14 years
Pore Volume	69,076,423 m³
Years @ 1 PVI	53.5 years
Permeability (k_x, k_y, k_z)	103 mD, 104 mD, 3.0 mD
Lorenz Coefficient	0.393
Recovery at 0.5 PVI	46.70%
Recovery at 1 PVI	70.60%
Recovery at 2 PVI	89.80%
Recovery at 10 years	18.70%
Recovery at 100 years	88.30%
Recovery at 1000 years	99.90%

Table A.6: Summary of key parameters and simulation results for Model L2.

Parameter	Value / Description
Model Name	L2 model
Grid Dimensions	121,121,121
Number of Layers (Z)	9
Injection Rate	3398 m³/day
Flow Rate	21.37 Mbbl/day
Breakthrough Time (INJ)	16.44 years
Breakthrough Time (PRD)	15.88 years
Pore Volume	61,914,601 m³
Years @ 1 PVI	50 years
Permeability (k_x, k_y, k_z)	92 mD, 96 mD, 1.1 mD
Lorenz Coefficient	0.44
Recovery at 0.5 PVI	45.00%
Recovery at 1 PVI	66.90%
Recovery at 2 PVI	86.10%
Recovery at 10 years	20.00%
Recovery at 100 years	86.10%
Recovery at 1000 years	99.90%

Table A.7: Summary of key parameters and simulation results for Model L3.

Parameter	Value / Description
Model Name	L3 model
Grid Dimensions	121,121,121
Number of Layers (Z)	23
Injection Rate	4547 m³/day
Flow Rate	28.6 Mbbl/day
Breakthrough Time (INJ)	10.81 years
Breakthrough Time (PRD)	10.67 years
Pore Volume	64,470,772 m³
Years @ 1 PVI	38.9 years
Permeability (k_x, k_y, k_z)	123 mD, 128 mD, 0.86 mD
Lorenz Coefficient	0.476
Recovery at 0.5 PVI	42.90%
Recovery at 1 PVI	64.50%
Recovery at 2 PVI	83.50%
Recovery at 10 years	25.60%
Recovery at 100 years	88.50%
Recovery at 1000 years	99.90%

Table A.8: Summary of key parameters and simulation results for Model L4.

Parameter	Value / Description
Model Name	L4 model
Grid Dimensions	121,121,121
Number of Layers (Z)	104
Injection Rate	5473 m³/day
Flow Rate	–
Breakthrough Time (INJ)	8.48 years
Breakthrough Time (PRD)	8.53 years
Pore Volume	62,361,223 m³
Years @ 1 PVI	31.2 years
Permeability (k_x, k_y, k_z)	149 mD, 154 mD, 0.86 mD
Lorenz Coefficient	0.507
Recovery at 0.5 PVI	42.50%
Recovery at 1 PVI	61.70%
Recovery at 2 PVI	78.70%
Recovery at 10 years	30.90%
Recovery at 100 years	87.30%
Recovery at 1000 years	99.90%